POLITECNICO DI TORINO
Repository ISTITUZIONALE

Numerical models comparison for fluid-viscous dampers: Performance investigations through Genetic Algorithm

Original
Numerical models comparison for fluid-viscous dampers: Performance investigations through Genetic Algorithm / Cucuzza, R.; Domaneschi, M.; Greco, R.; Marano, G. C.. - In: COMPUTERS & STRUCTURES. - ISSN 0045-7949. - 288:(2023), pp. 1-18. [10.1016/j.compstruc.2023.107122]

Availability:
This version is available at: 11583/2982815 since: 2023-10-06T10:56:07Z

Publisher:
Elsevier

Published
DOI:10.1016/j.compstruc.2023.107122

Terms of use:

This article is made available under terms and conditions as specified in the corresponding bibliographic description in the repository

Publisher copyright
Elsevier postprint/Author's Accepted Manuscript

© 2023. This manuscript version is made available under the CC-BY-NC-ND 4.0 license http://creativecommons.org/licenses/by-nc-nd/4.0/.The final authenticated version is available online at: http://dx.doi.org/10.1016/j.compstruc.2023.107122

(Article begins on next page)

14 May 2026

Numerical models comparison for fluid-viscous dampers: performance investigations through Genetic Algorithm

Raffaele Cucuzza[a], Marco Domaneschi[a,*], Rita Greco[b], Giuseppe Carlo Marano[a]

[a]*Politecnico di Torino, DISEG, Dipartimento di Ingegneria Strutturale, Edile e Geotecnica, Corso Duca Degli Abruzzi, 24, Turin, 10128, Italy*

[b]*Dipartimento di Ingegneria Civile, Ambientale, del Territorio, Edile e di Chimica, Politecnico di Bari, via Edoardo Orabona, 4, Bari, 70126, Italy*

Abstract

Fluid-viscous dampers played a crucial role in the protection of new or existing buildings against external actions as earthquakes and winds. In the last decade, several investigations have been conducted aiming to develop accurate numerical models. However, none has been focused on a comprehensive comparisons between the most used fluid-viscous damper models considering the variability of their parameters in a mass-production series.

In this paper, an identification procedure has been performed by comparing nine different existing literature models with the objective of evaluating their ability to match experimental loops of mass-produced fluid-viscous devices, both in terms of accuracy and robustness. Indeed, the model that is most effective for reproducing the characteristic of a specific specimen may not be representative (i.e., showing larger parameters variability) of the mass production of the same device type. For this purpose, dynamic tests have been developed in the laboratory and the experimental outputs have been adopted as the target function of the procedure. The identification scheme has been designed by implementing an optimization procedure via Genetic Algorithm. Results demonstrate how differential laws better fit the experimental cycles with respect to algebraic ones, and also show how few models in the series can offer a high level of both accuracy and robustness.

Keywords: Viscous Damper, Numerical model, Optimization, Genetic Algorithm, Statistical Analysis, Mass-production

1. Introduction

The significance of civil engineering structures in societal development cannot be overstated, as they form the backbone of transportation systems, utilities, and habitation. How-

*Corresponding author.

ever, these structures encounter formidable challenges arising from external actions, notably seismic events, which pose substantial risks of damage and functional impairment [1, 2, 3, 4]. Consequently, the adoption of resilient design principles, specifically the integration of damping devices [5, 6, 7, 8, 9], assumes paramount importance in safeguarding these structures, enabling their continued operation even amidst severe seismic events of greater intensity [10, 11, 12].

Fluid-dynamic damper technology is a mature technology that has been extensively studied and incorporated into anti-seismic design standards and guidelines in many countries worldwide [13, 14, 15, 16]. For example, the Japan Society of Civil Engineers recommends the use of fluid-dynamic dampers in seismic-resistant design, and many buildings in Japan are equipped with these devices [17]. Similarly, the Council of Tall Buildings and Urban Habitat recommends the use of fluid-dynamic dampers in high-rise buildings located in high-seismicity areas [18].

The ability of fluid viscous dampers (FVDs) to dissipate a large amount of energy, the creation of forces that are out of phase with displacements, and the potential to improve damping ratios without significantly changing stiffness make them appealing. This is not the case with other devices as hysteretic ones. The military and aerospace industries were the first to demonstrate the efficacy and reliability of FVDs. This paved the path to the application of FVDs in civil engineering for both new and existing structures [19, 20].

Both experimental testing and numerical modelling are frequently used to characterize the mechanical properties of novel systems or devices. Although the former approach is more expensive than the latter, it directly leads to a physical understanding of the system and can therefore be used for final verification. Numerical simulation, in contrast, employs numerical techniques to quantitatively describe the development of a physical system and enables more economically exploring a wide range of potential design options. A satisfactory representation of the actual mechanical behavior of the understudied device can be obtained from such simulations by employing realistic models [21, 22]. By simulating the behavior of control devices, engineers can evaluate the qualities of different design solutions before implementing them in the physical structure. This can save time and money by avoiding costly trial-and-error processes and ensuring that the protection strategy is reliable and

efficient [23, 24].

The effectiveness of FVDs depends on various factors, such as the type and properties of the materials used, the geometry and structural configuration, and the external forces acting on the structure. Therefore, numerical simulations can be used to evaluate their efficiency and improve their performance [25, 26, 27, 28], also by reproducing their characteristic behavior in complex structural systems [29, 30].

Furthermore, numerical simulations can provide valuable insights into the behavior of control devices under extreme conditions that are difficult or impossible to replicate in physical experiments. For example, numerical simulations can be used to evaluate the behavior of control devices under earthquakes of different magnitudes and frequencies, or under wind speeds that are beyond the capabilities of physical experiments [31, 32].

Choosing the model to reproduce in operation the fluid-viscous device is a critical step for reasons mainly related to mass production of the devices. Indeed, the model identified on a single device could not be robust enough to represent the variability of the devices' characteristics that belong to the same mass production. On the other hand, a less accurate model identified on a tested device would more likely be reflective of the kind as a whole[33, 34].

Several papers can be found in the literature in which suitable numerical models for reproducing the cyclic behavior of FVD devices are developed. A first class is that of algebraic models that assemble spring-type stiffness elements and dashpot-type damping elements, linearly or nonlinearly proportional to displacement and velocity. The simplicity of these models favoured their widespread use [35, 36, 37], including within international standards (e.g. [38]) and among FVD device manufacturers. However, these models although having the advantage of being simple and requiring low computational efforts are not always accurate in reproducing the hysteretic behavior of control devices as FVD ones. On the contrary, a different class of models overcome the limitations of algebraic ones: they are the differential models of hysteresis. The Bouc-Wen model [39] has been widely used to simulate different hysteretic devices being able to display a broad range of cyclic behaviors (e.g., [40]). Similarly, the LuGre model [41] although originally designed for friction hysteretic devices has been developed to reproduce different dampers (e.g., [42]). Lu et al. [43] introduced

an unified differential model containing a number of variants to simulate different types of devices with some applications in the literature (e.g., [44]).

Although fluid-viscous dampers have been extensively studied in the literature with various practical applications in the real world, the aspect described regarding mass production and the identification of representative models has not yet been thoroughly investigated. The objective of this research is to close this gap by contributing to the evaluation of a variety of numerical models that have been used to replicate the characteristics of mass-produced fluid-viscous devices. This comparison is based on some dynamic laboratory tests performed on five samples of the same type of fluid-dynamic device. Parameter identification will be carried out through an optimisation procedure based on the use of Genetic Algorithms (GA). The result of the parameters identification for the different models, for the different tested devices, will be then studied through a statistical investigation aimed at determining the most robust and the most accurate numerical model.

The paper has the following organization. Section 2 collects the main numerical models involved in the optimization problem. A brief description of each model has been introduced and the main parameters discussed. In Section 3, the samples description and the laboratory equipment used for the dynamic tests has been described. Section 4 is devoted to the mathematical formulation of the problem and the description of the adopted optimization algorithm with regard to the analysis settings and stopping criteria. Section 5 collects the results of the optimization process and shows the optimal hysteresis cycles for each investigated model. In Section 6, the authors provide a statistical analysis in order to identify underlying trends and patterns. All the results derived from the analysis have been organized in Section 7, in which suitable indices concerning with the accuracy and the robustness of each model are adopted. The final discussion including future developments is provided in Section 8. Finally, Appendix A and B report the outputs of the optimization process.

2. Numerical models for fluid viscous dampers

In the literature different numerical models to simulate FVD characteristics can be found, with different formulations (e.g. differential or algebraic equations). Their parameters can be tuned through the definition of a goal (or cost) function to be minimized, within an

identification process, until a suitable level of accuracy is achieved.

The present section addresses the selection of existing numerical models for FVD starting with rheological models [33], moving up in complexity from the linear viscous damper to generalized models. Next, differential models are presented for simulating the experimental loops of FVDs in terms of force-displacement and force-velocity characteristics.

2.1. Linear viscous model - Law #1

The classic linear viscous model is the simplest way to represent a velocity-dependent mechanical law. When the FVD is modeled in this fashion and given a cyclic input, the force F produced by the relative velocity v with respect to the linear viscous damping parameter C is:

$$F(t) = Cv(t) \tag{1}$$

The key benefit of this fundamental model is that it is very straightforward, although occasionally it falls short of being an accurate description of actual mechanical behavior. The generalized (nonlinear) viscous model, which relies on a fractional exponent of the velocity rather than a straightforward linear relationship, has updated it as a result. The following section describes the generalized nonlinear viscous model.

2.2. Generalized viscous model - Law #2

The fundamental distinction between the classical and generalized models is that the latter incorporates nonlinearity in the spring and viscous components. Additionally, the coefficients of the generalized models' resistive forces are fractional exponential. The generalized nonlinear viscous model consists of two parameters: the linear viscous damping parameter C and the damping term exponent α, which is usually selected in the range $[0, 1]$.

$$F(t) = Csign(v(t))|v(t)|^{\alpha} \tag{2}$$

Distinct values of α are related to different mechanical behaviour. For example, the linear viscous damping law corresponds to $\alpha = 1$; if α assume values close to 0, the friction behavior is seen (consequently, the force increases quickly for small velocity values and becomes almost constant for large velocity values). Due to its effectiveness in predicting structural behavior,

this damping law has been widely adopted by different authors. For instance, Banazadeh et al. [45] research on a comparison of the seismic collapse performances of steel frames equipped with linear and nonlinear viscous dampers. Additionally, many structural computer routines and standard guidelines for reproducing FVDs reference to this law.

Experimental research, however, showed that the viscous dampers force varies on both damper relative displacement d and velocity v. Therefore, simulating such mechanical feature involves joining a spring element and a viscous element, respectively. The family of Kelvin-Voigt models is created if these two components are connected in parallel. The fundamental Kelvin-Voigt model, for instance, can be derived with a linear spring and a straightforward linear dashpot in parallel. Other behaviors are produced when nonlinear springs are coupled with generalized nonlinear viscous models.

Both linear and parabolic models for the elastic force F_e can be expressed as:

$$F_e(t) = K_1 d(t) \tag{3}$$

$$F_e(t) = K_2 d(t)^2 + K_1 d(t) + k_0 \tag{4}$$

where K_1 is the elastic stiffness, K_2 and K_0 are two constants. The parabolic function reproduces the test cycle shape better, but the linear function may be preferable because it is less complicated and generates a similar energy balance [46, 47].

2.3. Generalized viscous and linear elastic model - Law #3

The equation of motion for a generalized Kelvin-Voigt model subject to a time-varying force p is obtained by combining Equations 2 and 3:

$$F(t) = K_1 d(t) + C sign(v(t)) |v(t)|^{\alpha} \tag{5}$$

2.4. Generalized viscous and quadratic elastic model - Law #4

The combination of the generalized viscous model in Equation 2 with the parabolic model for the elastic force in Equation 4 (without considering the contribution of K_0) allows

to define the generalized viscous and quadratic elastic force:

$$F(t) = K_1 d(t) + K_2 d(t)^2 + C sign(v(t))|v(t)|^{\alpha} \tag{6}$$

2.5. Generalized Kelvin-Voigt model - Law #5

The models previously described as function of displacement and relative velocity computed with respect to the connection points of the FVD device can be further generalized by defining the so-called Kelvin-Voigt model. Following this approach, the spring and the viscous components both involve nonlinearities. Consequently, in this generalized model, the device force is represented by two exponential components.

$$F(t) = K sign(d(t))|d(t)|^{\beta} + C sign(v(t))|v(t)|^{\alpha} \tag{7}$$

2.6. Bouc-Wen model of hysteresis - Law #6

The Bouc-Wen endochronic model has been chosen to simulate the hysteretic component of a broad class of control devices since it is perhaps the most eclectic phenomenological model of hysteretic mechanical systems given by the current literature. This decision is backed by the model's consistency in both mathematics and physics as well as by the outstanding agreement between experimental and numerical data [48, 28].

The control force generated by the Bouc-Wen model of hysteresis can be defined as

$$F(t) = \alpha K d(t) + (1 - \alpha) K z(t) + C v(t) \tag{8}$$

Where $z(t)$ is the variable which allows to define the hysteretic behavior, K is the pre-yielding stiffness of the model, α is the pre-post yielding stiffness ratio ($\alpha = 1$ is associated to the elastic response, while $\alpha = 0$ to the perfectly plastic response. To introduce a linear viscous contribution, it is possible to define a component proportional to velocity according to the constant C. The hysteretic variable $z(t)$ is introduced by defining the differential component of the model as follows.

$$\frac{dz(t)}{dt} = A v(t) + \beta v(t)|z(t)|^n - \gamma |v(t)|z(t)|z(t)|^{n-1} \tag{9}$$

Where A, β, γ, n are constant with time parameters which regulate the the hysteresys cycle shape and amplitude (dissipation level), the unloading branch linearity and the transition smoothness between the pre-yielding and the post-yielding phase. In detail parameter A is associated to the initial stiffness, β drives the hysteresis amplitude (the dissipation intensity), γ regulates the unloading path in the cyclic behavior, while n the transition smoothness. The efficiency of the model (e.g., stability, consistency, passivity, admissibility) can be verified by assuming suitable values for the parameters, while the identification procedure for the characteristic parameters can be simplified assuming $\beta = \gamma$, $A = n = 1$ [49, 28].

2.7. Unified model for visco-elastic type devices - Law #7

For simulating the hysteretic behavior of various types of dissipative devices, Lu et al. [43] proposed a unified analysis model with the internal variable $z(t)$. The model may imitate many device kinds by giving the internal variable various physical meanings. The summary of the viscoelastic type is presented in this section, while friction dampers are the subject of the following one. The visco-elastic control force associated to the damper is computed as follows.

$$F(t) = K sign(z(t))|z(t)|^{\beta} \tag{10}$$

$$\frac{dz(t)}{dt} = -sign(z(t)) \left(\frac{K|z(t)|^{\beta}}{C} \right)^{\frac{1}{\alpha}} + v(t); \tag{11}$$

Where K is the stiffness of the elastic component, C the damping coefficient of the viscous element, α and β exponential coefficients.

2.8. Unified model for friction type devices - Law #8

The force-displacement characteristic of the device interested in reproducing in the present study, with a rapid transition between elastic and plastic phases, coupled with a rectangular-trapezoidal shape of hysteretic cycles, suggests that dissipative models normally used for friction control devices should also be considered in the identification process. So this section and the next are devoted to two types of models for friction type devices found in the literature. For simulating the friction dissipative control force, Lu et al. [43] reported the following unified analysis model.

$$F(t) = z(t)\mu N \tag{12}$$

$$\frac{dz(t)}{dt} = \left(\frac{K}{\mu N}\right) sign(1 - INT(|z(t)|)sign(z(t)v(t)))v(t) \tag{13}$$

Where μ is the friction coefficient, N the normal contact force, K the device axial stiffness, $INT(x)$ is the integer part function of variable x.

2.9. LuGre model of hysteresis - Law #9

The so-called LuGre model was proposed by Canudas et al. [50] to explain friction dynamics. This model has been then developed applied in a variety of contexts, also different from the type of friction-related devices [41, 51]. The LuGre model is an effective solution to model and control design problems due to its mathematical simplicity and accuracy. The control force exerted by the damper can be computed as follows.

$$F(t) = \beta z(t) + CV(t) + Kd(t) + \epsilon \frac{dz(t)}{dt} + F_0 \tag{14}$$

$$\frac{dz(t)}{dt} = v(t) - \alpha|v(t)|z(t) \tag{15}$$

Where K is the stiffness paramenter, C the damping coefficient, and α, β, ϵ allow to define the cycles characteristics (i.e., amplitude and shape). For the aim of this identification problem ϵ, K and F_0 can be assumed with zero values [51, 41].

3. Description of the laboratory tests

In the SISMALB srl laboratory in Taranto, Italy, five samples of the same 300kN FVD series (Figure 1) was tested. Table 1 reports the FVDs design conditions.

Table 1: Fluid viscous damper design conditions

F[kN]	Stroke [mm]	d_{design} [mm]	V_{max} [mm/s]	α
292 ± 55	± 55	± 45	500	0.3

The SISMALAB test equipment consisted of a high-resistance steel frame that can support loads of 2200 kN in both tension and compression. The FVD was connected by pins to the frame structure and to the actuator, which can be both force- or displacement-controlled (Figure 2).

A 2500kN load cell was placed between the actuator and the FVD specimen to measure the cyclic forces throughout the experimental tests, while a transducer was used to measure the device movements. In a displacement-imposed test, the device movements are controlled by a transducer mounted on the device. The control and data acquisition system is able to generate real-time analysis of device displacements by instantaneous variation of applied forces by the servant cylinder, by means of a computer automatic control hydraulic pressure system. The displacement–time history should be imposed with different laws, from sinusoidal to triangular as well as ramped or through a generator step of generic ones. Acquiring systems have 30 channels and can command two actuators at the same time.

The FVD specimens were tested using the transducer output as feedback for the closed-loop displacement control. More in detail, the database is composed of 24 tested devices with the same properties and set-up adopted during the test. The laboratory provided the results of the pressure test related to 5 devices that were identified with a specific ID serial number. For each device, the test has been performed by applying an internal pressure over 275 bar and has been maintained for at least 120s. Moreover, all tests considered in the experimental campaign have been carried out by applying six sinusoidal cycles characterized by a specific ratio of the maximum velocity corresponding to low velocity (lower than 1%), 1%, 25%, 50%, 75% and 100% of the maximum design value. Finally, for each device, the damping efficiency at 100% of the maximum velocity has been tested by applying 10 sinusoidal cycles. Table 2 reports the test conditions for the five selected FVD specimens with specific regard to the last configuration in order to assess the damping capacity. Maximum, $Load_{max}$, and minimum load, $Load_{min}$, experienced during the test as well as maximum, d_{max}, and minimum displacement, d_{min}, have been reported. Consistent with what was said before, tests selected by the database consisted of 10 sinusoidal cycles with 40mm amplitude at 0.5m/s.

Table 2: Fluid viscous damper test conditions

No.	$Load_{max}/Load_{min}$ $[kN]$	d_{max}/d_{min} $[mm]$	Cycles
$Test_1$	327/-317	44/-43	10
$Test_2$	318/-308	45/-43	10
$Test_3$	267/-259	44/-43	10
$Test_4$	289/-282	43/-42	10
$Test_5$	283/-284	44/-42	10

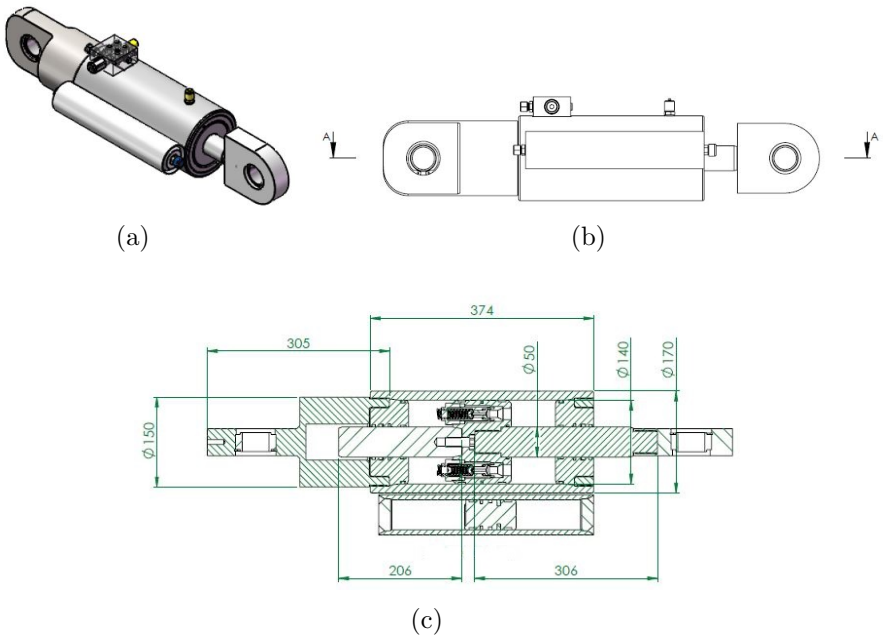

(a) (b) (c)

Figure 1: 3D model of FVD test device (a); Longitudinal view of the FVD test device (b); Trasversal section of FVD test device (c)

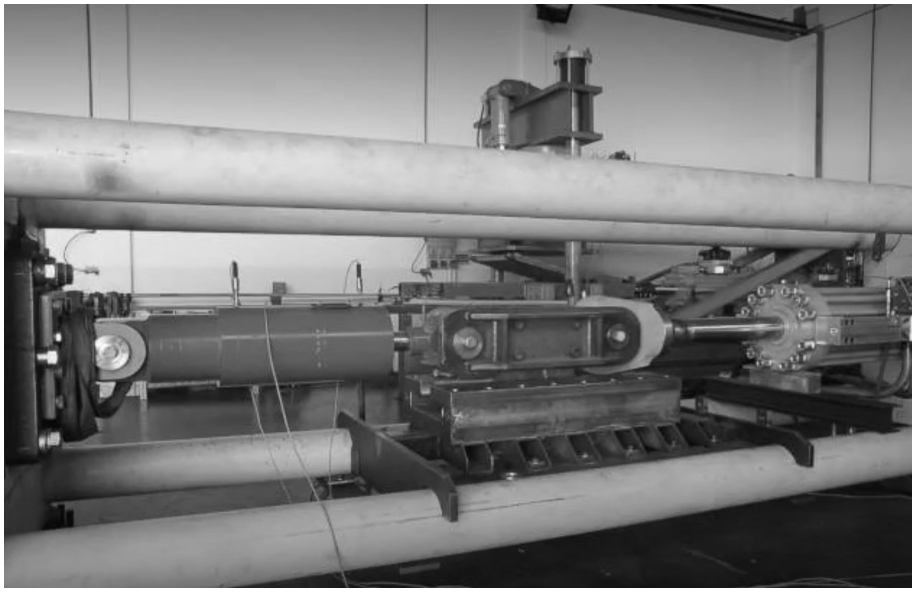

Figure 2: FVD specimen on the test facility at SISMALAB

4. Identification scheme and analysis setting

In this section, the mathematical formulation of the optimization problem is introduced. Specifically, the Objective Function (OF) and the design variable are defined. Therefore, both the setting criteria and the Genetic Algorithm (GA) for the optimization process are illustrated.

4.1. Mathematical formulation

The parameters identification requires to solve an unconstrained optimization problem and a suitable objective function (OF) has to be minimized.

All the selected constitutive models depend on different parameters, which become the components of the design variable vector x. The model parameters are identified by solving the following single-objective optimization problem:

$$\textbf{Minimize} \quad W = f(x_i), \quad i = 1, ..., n \tag{16}$$

$$\textbf{Subject to} \quad x_i^l \leq x_i \leq x_i^u \tag{17}$$

where x=$\{x_1, ..., x_j, ..., x_n\}$ represents a set of real parameters which depends on the adopted numerical model. The size of this vector, hence, is related to the number of variables which govern the constitutive law. The x^l=$\{x_1^l, ..., x_j^l, ..., x_n^l\}$ and x^u=$\{x_1^u, ..., x_j^u, ..., x_n^u\}$ vectors represent the lower and upper bounds of x, respectively. In this way, the domain of feasible solutions is restricted to a sub-domain in which x can assume the values between x^l and x^u. For the aim of this research, a suitable OF has been defined in the integral form as follows:

$$f(x) = \frac{1}{\sigma_{p_m}(t_{end} - t_{start})} \int_{t_{start}}^{t_{end}} abs(p_m - p_e(x))dt \tag{18}$$

where t_{start} and t_{end} are the start and end time records, respectively, and $p_m(t)$ is the experimentally measured force, while $p_e(t)$ is the estimated force.

The Matlab ODE45 function has been used for solving the (nonstiff) ordinary differential problem. The procedure implemented by the solver is the Runge-Kutta method. The fixed time step for the solution procedure is the sampling time step adopted during the laboratory test. This procedure was adopted for only the differential laws (from law#6 up to law#9)

In order to reduce the computational effort during the optimization process or avoid critical values generating numerical noises, lower, x^l, and upper, x^u, bounds for each design variable are carefully fixed, detecting more suitable ranges of variability. In this way, no interest solutions are discarded, and the efficient exploration phase of the algorithm is guaranteed.

4.2. GA algorithm and analysis setting

In order to solve the problem stated in the previous section, a real-coded GA is adopted. This is a population-based stochastic optimization technique appropriate for global optimization, which does not require direct evaluation of gradients. Introduced by John Holland [52], it is inspired by Charles Darwin's theory of natural evolution. This algorithm reflects the process of natural selection where the fittest individuals, also called parents, are selected for reproduction in order to produce offspring of the next generation. At the end of the process, the best survival among all the fittest candidates found at each generation is selected as the best globally optimized solution. Although the native GA worked with binary values representing genes, encoded in string structures called chromosomes, in this paper the authors overcome the limits related to the decoding process by using a real-code GA in which genes and chromosomes represent directly the design variables and the solutions of the problem.

At each iteration, traditional GA phases were adopted during the optimization as following:

- **Initial population**: in this phase, individuals with a set of random genes (x_i) composing chromosomes (x) are created by observing lower and upper bounds reported in table 4. Gene represents, at each generation, the candidate value of a specific design variable involved in the identification procedure. A set of genes (vector form) represent a solution of the problem for the current generation. In this way, the best solution is selected and the optimal set of parameters which govern that specific law is detected.

- **Fitness function**: in this phase, the fitness of the candidate solutions is evaluated by calculating the OF introduced in the previous section 4.1.

- **Selection**: During this phase, a Roulette Wheel Selection was implemented in order to guarantee that the two fittest parents are selected for the next steps. Adopting this technique, a probability to each parent is assigned and the parents with higher fitness are more likely to be chosen for the next steps.

- **Crossover**: in this phase, a uniform random crossover was performed in which recombination of gene pool between parents is performed in a random way. Lower and upper bounds are imposed at this stage such that if only a gene of the new offspring

is not ranged within the imposed interval (higher than the maximum value or lower than the minimum value of that specific parameter), it is forced to assume maximum or minimum value, respectively.

- **Mutation**: aiming to improve the exploration and exploitation ability of the algorithm, a mutation rate of 1% is assigned. In this way, new genes are introduced into the population by modifying the gene pools of parents in a random way.

At the end of these stages, a sorted function was implemented aiming to store survivors with the best fitness among the generated offspring, at each generation. For this purpose, an elitism algorithm was adopted in order to copy the best chromosome of the previous population to the new one. The identification procedure can be considered ended when the stopping criteria of the algorithm are satisfied and the optimal set of parameters for each law is found. The entire procedure was run n times in order to check the reliability and robustness of the algorithm. Specifically, the authors observed that stagnation usually occurred for the algebraic models while no differential ones needed to use all the available 200 generations.

For clarity and repetitive purposes, the settings of the adopted algorithm and the stopping criteria are listed in table 3.

Table 3: Setting of the GA for each law

Pop. size	N.Generation	Evaluation	N. Run	Stagnation
200	200	40.000	20	20

Though a maximum of generation equal to 200 is set, stopping criteria occurs if OF value remains the same for 20 subsequent generations. In this way, the computational effort was reduced if stagnation is recognized.

In Table 4, the design variables of the optimization problem with their corresponding lower and upper bounds are reported.

5. Parameter identification results and cyclic behavior reproduction

In this section, the performance of the selected numerical models in reproducing the cyclic behavior of the tested FVDs has been analysed. Appendix A reports the mean and the standard deviation values of the design variables and the OFs for each investigated law.

Table 4: Lower and upper bounds of models' parameters

		x	
		x^l	x^u
Law #1	C **[kN/(mm/s)]**	0.0	2.0
Law #2	C **[kN/(mm/s)]**	0.0	2.0
	α **[-]**	0.0	1.0
Law #3	C **[kN/(mm/s)]**	0.0	2.0
	α **[-]**	0.0	1.0
	K_1 **[kN/mm]**	0.0	200.0
Law #4	C **[kN/(mm/s)]**	0.0	2.0
	α **[-]**	0.0	1.0
	K_1 **[kN/mm]**	0.0	300.0
	K_2 **[(kN/mm)^2]**	0.0	300.0
Law #5	C **[kN/(mm/s)]**	0.0	2.0
	α **[-]**	0.0	1.0
	K **[kN/mm]**	0.0	1000.0
	β **[-]**	0.0	5.0
Law #6	C **[kN/(mm/s)]**	0.0	0.3
	K **[kN/mm]**	30.0	100.0
	α **[-]**	0.0	1.0
	β **[1/mm]**	0.0	5.0
Law #7	C **[kN/(mm/s)]**	3.0	10.0
	α **[-]**	0.05	0.3
	K **[kN/mm]**	50.0	200.0
	β **[-]**	0.2	0.4
Law #8	C **[kN/(mm/s)]**	0.1	0.3
	K **[kN/mm]**	10	50
	μ **[-]**	0.1	1
	N **[kN]**	250	450
Law #9	C **[kN/(mm/s)]**	0.0	0.3
	α **[1/mm]**	0.0	2.0
	β **[kN/mm]**	20	100

Because of the reasonably high accuracy of the results in terms of OF, Test 2 has been considered to compare the hysteresis cycles of the different models against the laboratory tests. To avoid burdening the results description of the plots carried out by the optimization process, Appendix B reports the comparison between experimental and numerical force time-histories (F vs t_{vec}) for each model with specific regards to device 2.

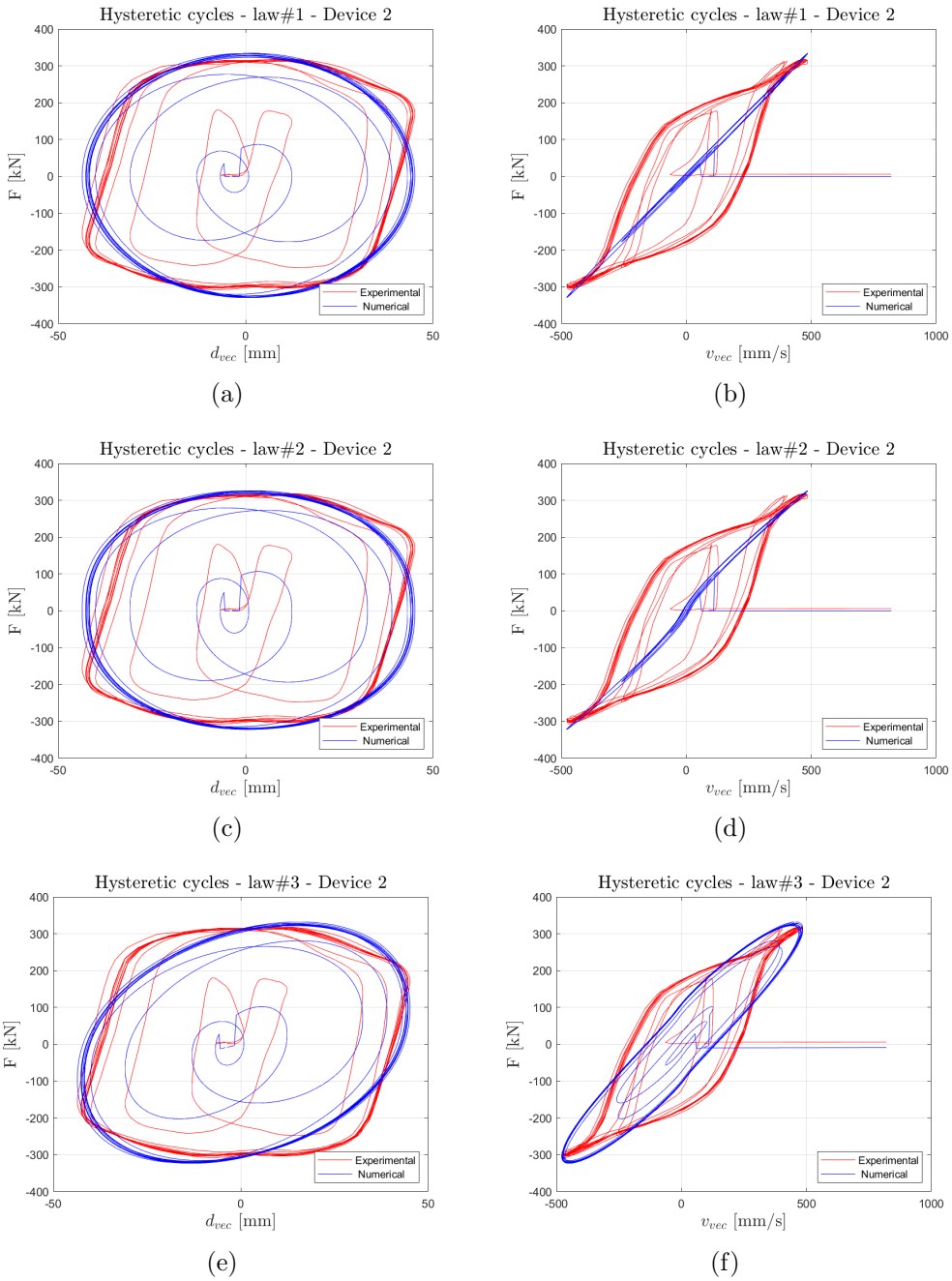

Figure 3 depicts the comparison of the force-displacement and force-velocity cycles for the nine numerical models considered against the device 2 laboratory results. A macroscopic difference between the first five models and the next four ones in reproducing the physical

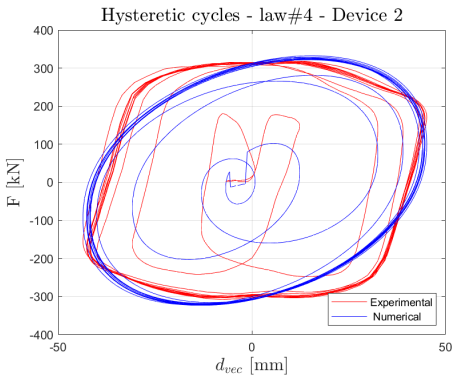

(g)

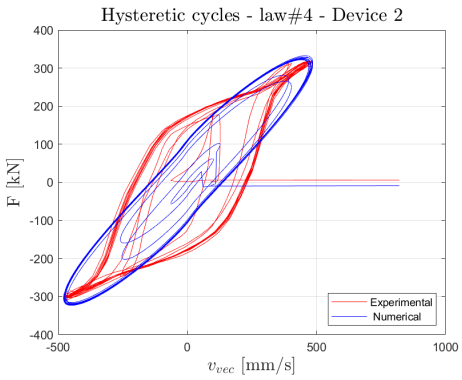

(h)

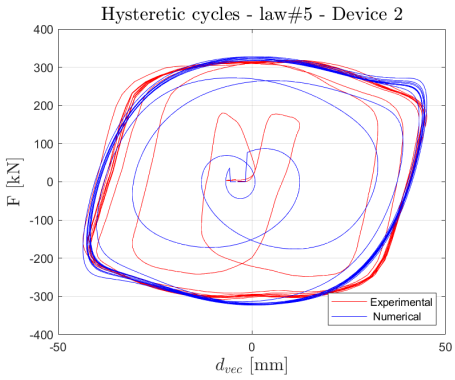

(i)

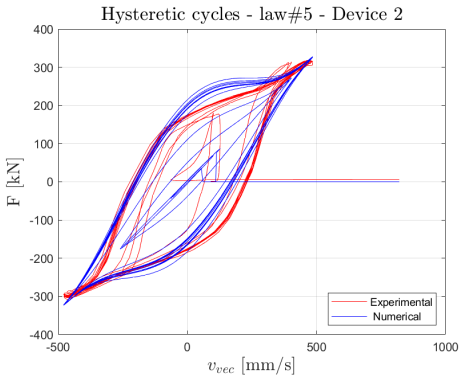

(j)

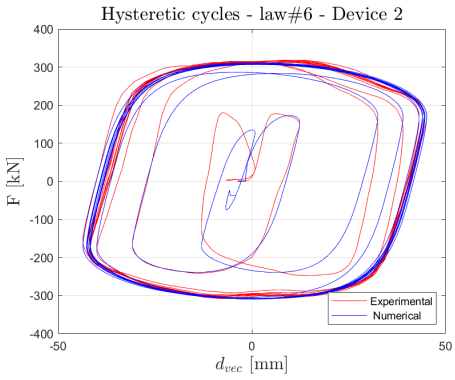

(k)

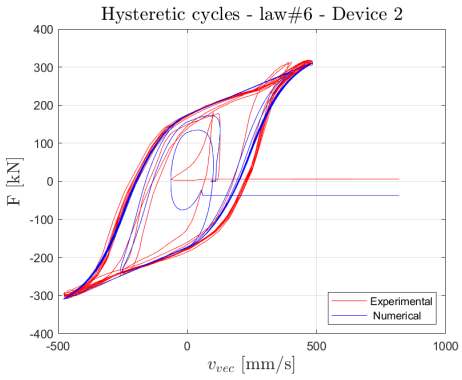

(l)

phenomenon is highlighted.

The first five algebraic models composed by different elementary features (elastic and damping elements with different characteristics) are the simplest and the most computationally inexpensive. The first two models (Fig.s 3 a-d) are evidently the least efficient in reproducing the cyclic response of the device: the exclusive presence of the damping component in the laws does not allow to reproduce the asymmetric shape of the force-displacement characteristics. Focusing on the force-velocity cycles, again the exclusive velocity proportional component of the force, with linear or nonlinear expression, still fails greatly in reproducing

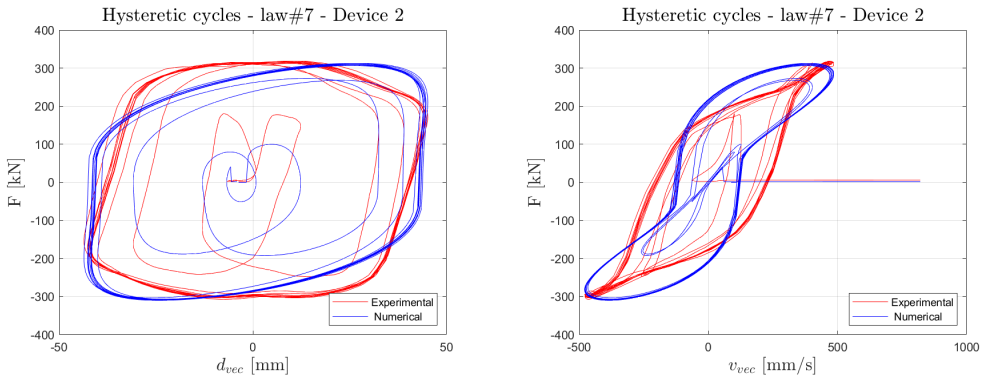

(m)

(n)

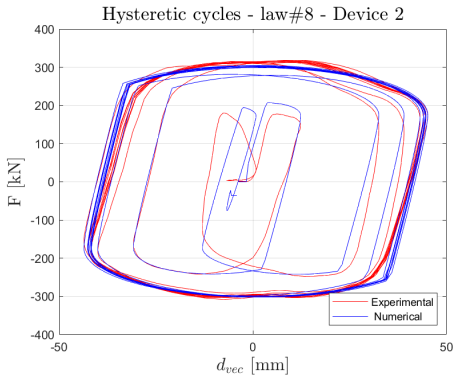

(o)

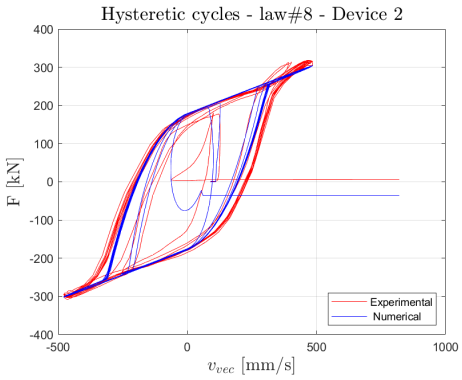

(p)

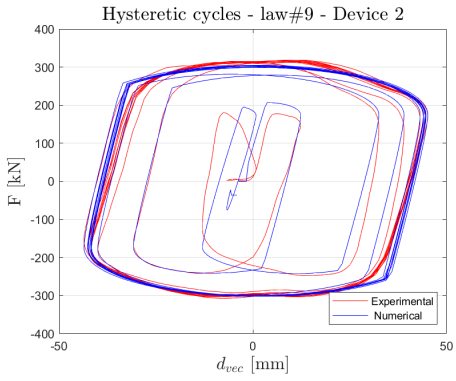

(q)

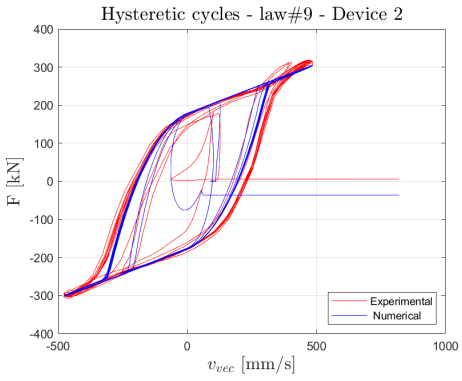

(r)

Figure 3: Comparison between theoretical and experimental force-displacement relationships (referred to Fig.s (a)-(c)-(e)-(g)-(i)-(k)-(m)-(o)-(q)) and force-velocity relationships (referred to Fig.s (b)-(d)-(f)-(h)-(i)-(l)-(n)-(p)-(r)) for law 1 up to law 9 with specific regard to Test 2

the response.

From the third model to the fifth (Fig.s 3 e-j), due to the introduction of the elastic elements, an improvement in reproducing the cycles is observed. However, only model number five (Fig.s 3 i-j) succeeds for the first time in qualitatively following the shape of both force-displacement and force-velocity cycles.

Focusing on the response of the last four models (Fig.s 3 k-r), an improved efficiency in simulating the behaviour of FVD devices is highlighted. However, this positive outcome is achieved at the price of a higher computational burden. Indeed, differential models are substantially more complex to process in terms of computational time than algebraic models.

However, the model related to Law #7 (Fig.s 3 m-n) does not appear satisfactory in its ability to reproduce the characteristic of FVDs, even from a qualitative observation, either as force-displacement or velocity-displacement. The optimization process has never been able to improve this result, despite different attempts.

The friction model (Fig.s 3 o-r) is qualitatively the most accurate in simulating the cyclic response of the FVDs. The Bouc-Wen model, probably the most versatile among the literature options (Figures 3 k-l), also produces a satisfactory qualitative result, equivalent to the ones from the friction models.

Generally, it is evident that none of the algebraic models is capable of reproducing the transient branch of hysteresis cycles at the beginning and final phases. On the contrary, among differential models, law#6, law#8 and law#9 exhibit a good grade of match not only at the full-capacity phase but also during the transient one. This result is demonstrated by the comparisons between experimental and numerical F vs t_{vec} curves reported in Appendix B.

6. Statistic analysis and discussion

In this section, the collected data from the optimization process for the adopted numerical models have been examined in order to identify underlying trends and patterns.

Fig.4 reports the bar graphs of the OF mean distribution and standard deviation for each tested FVD device considering the nine numerical models of hysteresis. In detail, the graphs represent the accuracy (Fig.4-(a)) of the models in reproducing the laboratory

tests, and their robustness (Fig. 4-(b)), respectively. In detail, Fig.4-(a) highlights the laws that are able to reduce the difference, or the error, between the variable that has been measured in the laboratory and that one computed as the optimal numerical solution. A low value of OF for a specified law means that the corresponding model is capable of fitting the experimentally measured force with reasonable accuracy. The best performers are represented by the differential laws, in particular Laws #8 and #9. However, the higher accuracy is obtained at the cost of higher computational burden, as already discussed, but mostly at the cost of lower robustness (higher standard deviation of, e.g., Laws #8 and #9, with respect to Law #1). This means that the law that is most accurate in reproducing the single physical phenomenon (i.e., the specific FVD) is also the one that shows the highest variability among samples of the devices in the same production series. However, it is worth noting that the intensity of the standard deviation is still small compared to the mean intensity. In order to emphasize the trend of standard deviation σ among the investigated laws, a logarithmic scale was adopted in Fig.4-(b). As expected, by increasing the complexity of the model from the algebraic to differential models, the dispersion index σ becomes higher except for Law#9 for which standard deviation, especially for Device#3, #4 and #5, assumes quite moderate values. Once that preliminary considerations are pointed out concerning

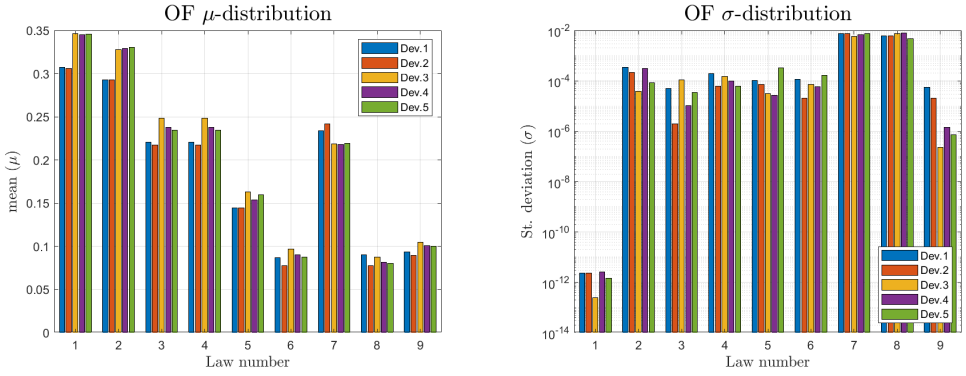

(a) (b)

Figure 4: OF mean (μ) distribution for each test devices (a); OF standard deviation (σ) distribution for each test devices (b). For each law, ($X - axis$), different colours are used for detecting the corresponding device.

with the global accuracy and robustness of each model, the authors focused on identifying the dispersion degree of each parameter for each law. In this way, a measure of the parameter which mostly affects the overall robustness can be assessed.

The models performance observed in terms of OF in Fig. 4 can be deepened by Fig.s 5-

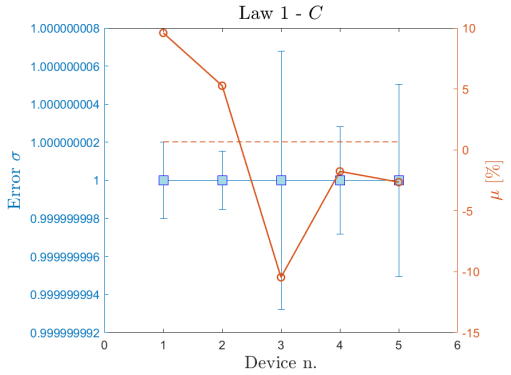

Figure 5: Normalized standard deviation and mean distribution of the identified damping C for the law 1. The left $y-axis$ shows the error bar of the standard deviation (σ), while the right $y-axis$ the percentage variation of mean distribution (μ). Dotted line represents the mean reference value among all five mean values evaluated for each Device.

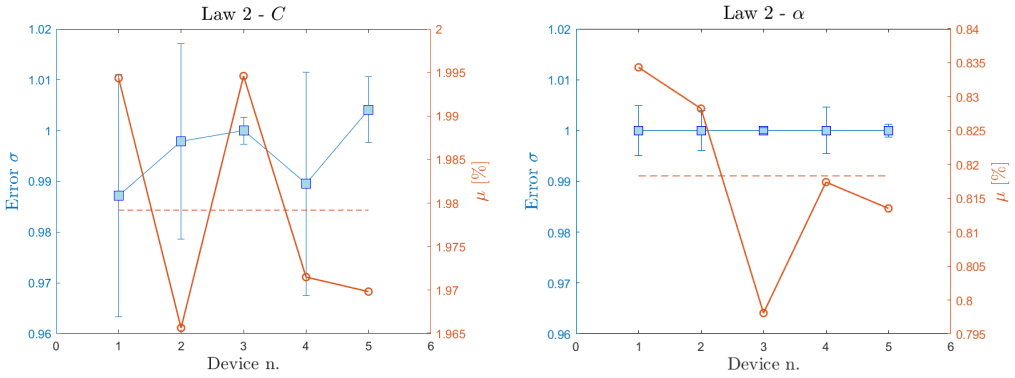

(a) (b)

Figure 6: Normalized standard deviation and mean distribution of the identified damping C (a) and control parameter α (b) for the law 2. The left $y-axis$ shows the error bar of the standard deviation (σ), while the right $y-axis$ the percentage variation of mean distribution (μ). Dotted line represents the mean reference value among all five mean values evaluated for each Device.

13. They present the statistics of the identified parameters, for the different models adopted and for the tested FVDs. In particular, each graph shows a double vertical axis, on the left the standard deviation of the considered parameter with respect to the mean (error bar of the standard deviation - *Error* σ) is reported, while on the right axis each figure shows the percentage variation of the mean of the considered parameter (calculated over the range of 20 performed optimization runs) with respect to the reference mean value (red dotted line) evaluated as the mean of all means value for each device.

Due to the fact that optimal parameters values obtained among the 20 runs show null variability, the authors decided to calculate the standard deviation σ with respect to the mean value of all runs for each device. This is demonstrated by the fact that all *Error* σ bars are centred to value 1 with the exception of Law#2 in which a tiny variability of

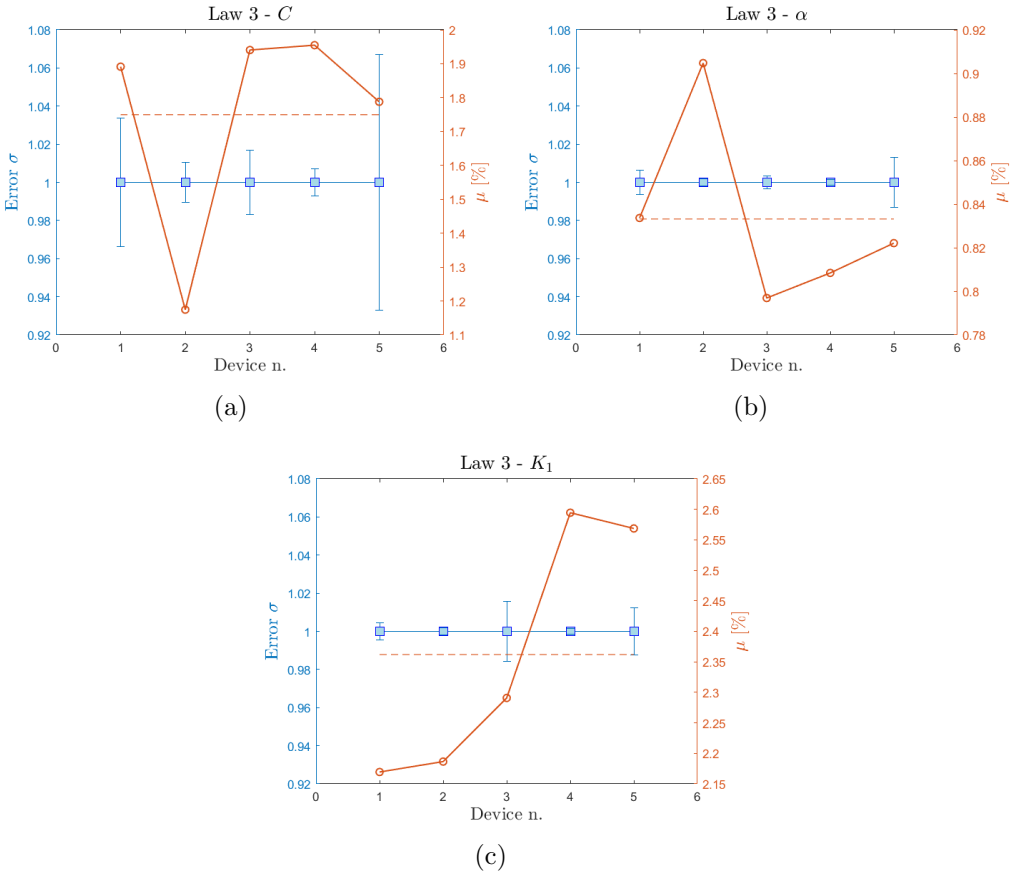

Figure 7: Normalized standard deviation and mean distribution of the identified damping C (a), control parameter α (b) and stiffness parameter k_0 (c) for the law 3. The left $y-axis$ shows the error bar of the standard deviation (σ), while the right $y-axis$ the percentage variation of mean distribution (μ). Dotted line represents the mean reference value among all five mean values evaluated for each Device.

parameter C can be recognized (see Fig.6-(a))

Therefore, the intensity scale of *Error* σ belonging to the same law has been uniformed. However, because of the high variability of μ parameter, right vertical axis, among different plots of the same law, it has not been possible to uniform. In this way, the identification of parameter(s) that mostly affects the overall dispersion of the law has been facilitated.

According to the trends observed in Fig.4-(b), *Error* σ range of values, represented by maximum and minimum values, increases from 1.0/0.92 (Law#1) up to 2.5/-0.5 (Law#5) with specific regard to algebraic laws.

The same trend is observed with respect to differential laws (Law#6 up to Law#9). However, differently from algebraic laws in which only one parameter is responsible for the entire dispersion of the law, several parameters show significant variability. In this sense, interesting considerations can be revealed by comparing Fig.10 and Fig.11. Though the range variability decreases from Law#6 to Law#7, the number of parameters with a significant

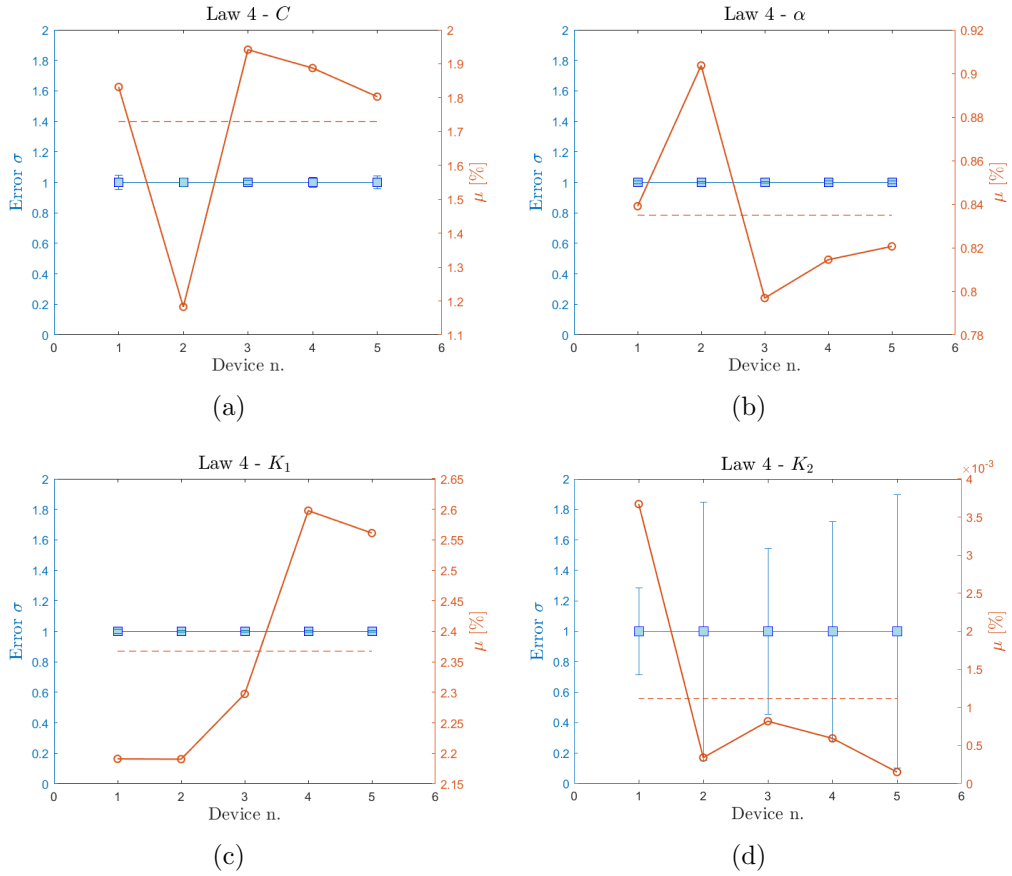

Figure 8: Normalized standard deviation and mean distribution of the identified damping C (a), control parameter α (b), stiffness parameter k_0 (c) and constant coefficient k_1 (d) for the law 4. The left $y-axis$ shows the error bar of the standard deviation (σ), while the right $y-axis$ the percentage variation of mean distribution (μ). Dotted line represents the mean reference value among all five mean values evaluated for each Device.

error bar, for each device, increases. Compared with Law#6 in which the dispersion is entirely concentrated into parameter C, in Law#7 each parameter exhibits not-negligible value of the *Error* σ. That is also reflected by observing the growth in Fig.4-(b) in which an overall increase of σ is detected for each device. Finally, growth trend is interrupted by Law#9 for which dispersion among parameters has been reduced dramatically.

If the *Error* σ trend was clearly identified by the authors, several discrepancies between the general behaviour of OF bar histograms (Fig.s 4(a),(b)) and the percentage variation μ plots for each device (law Fig.s 5-13) have been detected. However, the authors are convinced that the high variability of parameters can be addicted to the capability of a model to fit with experimental outputs. High is the variability μ of a specific parameter, high is the ability to capture differences between devices. As proof of what has been said, the highest variability is recognized for differential models, especially for Law#7, Law#8 and Law#9.

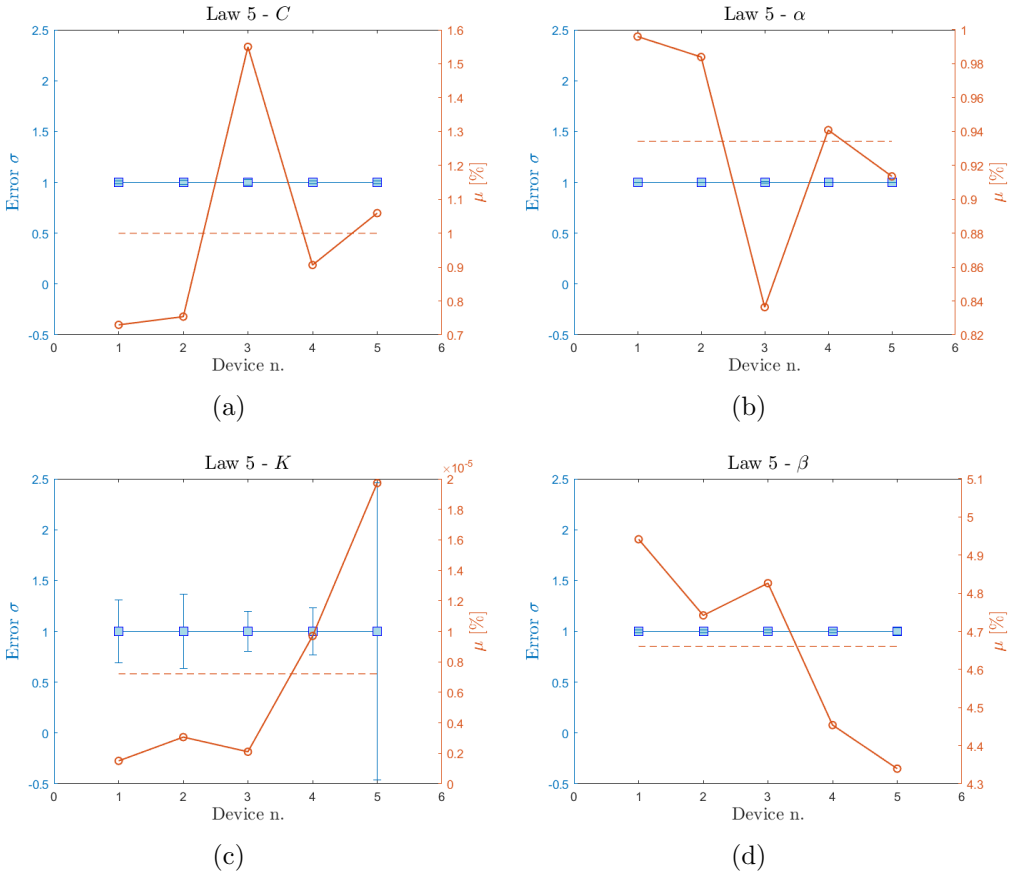

Figure 9: Normalized standard deviation and mean distribution of the identified damping C (a), exponent parameter α (b) and β (d) and stiffness parameter k_0 (c) for the law 5. The left $y-axis$ shows the error bar of the standard deviation (σ), while the right $y-axis$ the percentage variation of mean distribution (μ). Dotted line represents the mean reference value among all five mean values evaluated for each Device.

The high variability of μ, conceived as a good feature for a model in capturing changes in behaviour among the same devices, seems to fail when algebraic laws are treated. Indeed, though the variability of μ, especially for Law#1, results to be one of the highest among all sets of investigated models, the accuracy is not affected by sensible variation of this variable since the natively poor complexity of the models. In other words, the variability of parameters must not be allowed to outweigh the inner inefficiency of the model.

7. Pareto Front representation

In this section, the authors point out mathematical considerations to identify the best performer among the investigated models. As introduced in the previous Section 6, the goodness of each model has been evaluated in terms of accuracy (OF) and robustness (σ). If the former can be still assumed as representative of the global capability of a model to fit with experimental outputs, the latter gives a measure of how a single parameter can affect

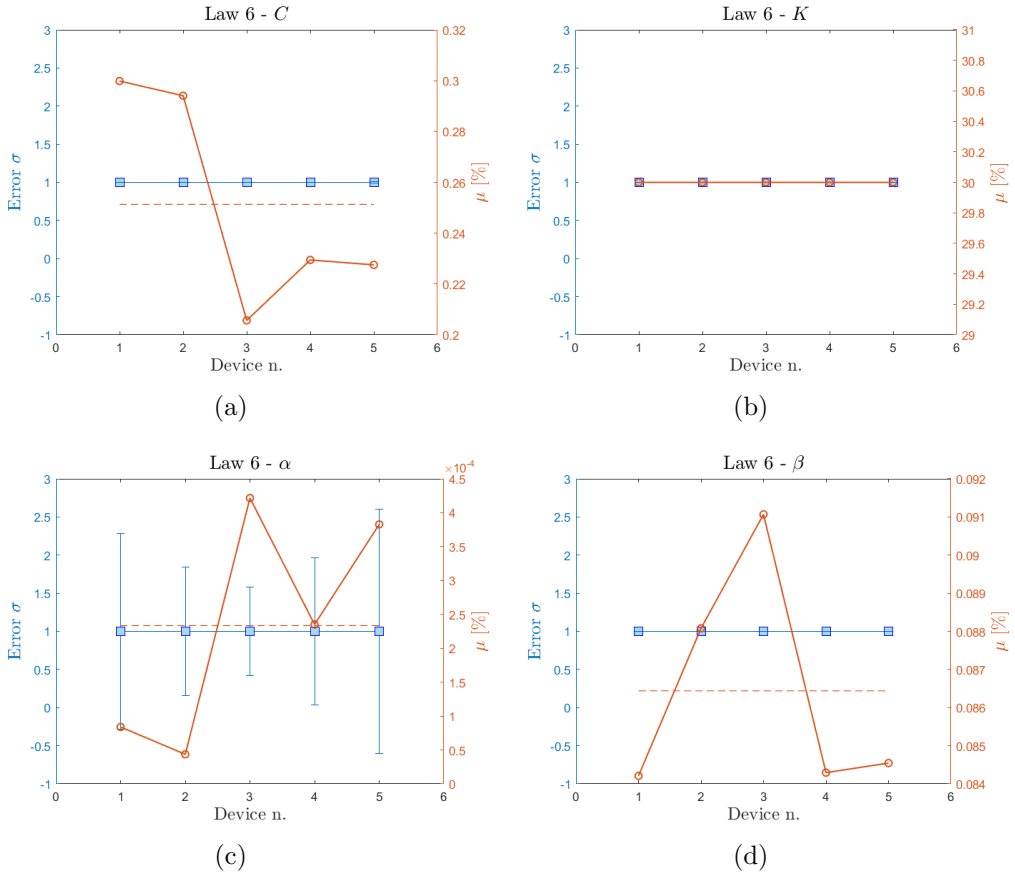

Figure 10: Normalized standard deviation and mean distribution of the identified damping C (a), stiffness parameter k_0 (b) and exponent parameter α (c) and β (d) for the law 6. The left $y-axis$ shows the error bar of the standard deviation (σ), while the right $y-axis$ the percentage variation of mean distribution (μ). Dotted line represents the mean reference value among all five mean values evaluated for each Device.

a specific model without any information about the overall robustness of that model.

For this reason, the authors introduce a new index β and the following mathematical procedure is adopted for its calculation.

At first, a matrix representation of parameters set for each low is derived in the following form:

$$\alpha = \left(\begin{bmatrix} \alpha_{11}^{(1)} & \alpha_{12}^{(1)} & \dots & \alpha_{1n}^{(1)} \\ \alpha_{21}^{(1)} & \alpha_{22}^{(1)} & \dots & \alpha_{2n}^{(1)} \\ \vdots & \vdots & \vdots & \vdots \\ \alpha_{m1}^{(1)} & \alpha_{m2}^{(1)} & \dots & \alpha_{mn}^{(1)} \end{bmatrix} \begin{bmatrix} \alpha_{11}^{(2)} & \alpha_{12}^{(2)} & \dots & \alpha_{1n}^{(2)} \\ \alpha_{21}^{(2)} & \alpha_{22}^{(2)} & \dots & \alpha_{2n}^{(2)} \\ \vdots & \vdots & \vdots & \vdots \\ \alpha_{m1}^{(2)} & \alpha_{m2}^{(2)} & \dots & \alpha_{mn}^{(2)} \end{bmatrix} \dots \begin{bmatrix} \alpha_{11}^{(j)} & \alpha_{12}^{(j)} & \dots & \alpha_{1n}^{(j)} \\ \alpha_{21}^{(j)} & \alpha_{22}^{(j)} & \dots & \alpha_{2n}^{(j)} \\ \vdots & \vdots & \vdots & \vdots \\ \alpha_{m1}^{(j)} & \alpha_{m2}^{(j)} & \dots & \alpha_{mn}^{(j)} \end{bmatrix} \right) \tag{19}$$

Vector α collects all parameters ($\alpha_{m,n}$) in matrices. Each matrix is representative of a specific law (j).

The first index, m, and the second index, n, of the generic identified parameter $\alpha_{m,n}$ represent

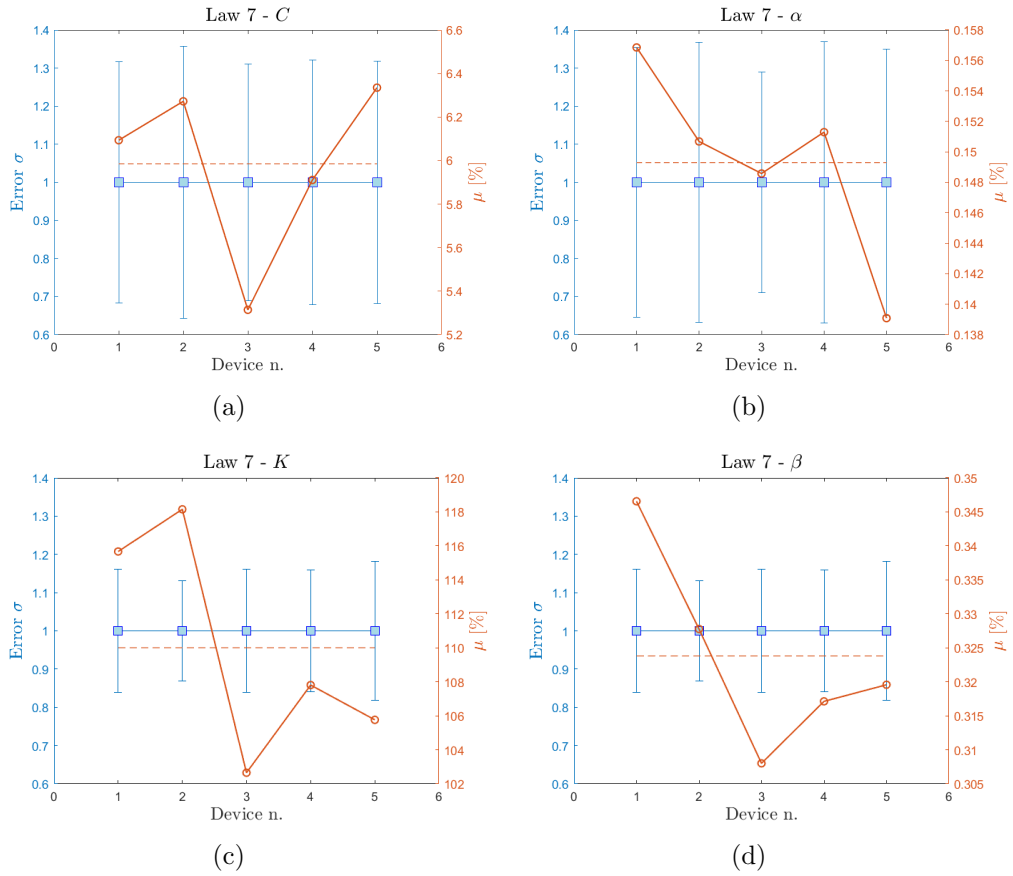

Figure 11: Normalized standard deviation and mean distribution of the identified damping C (a), exponent parameter α (b) and β (d) and stiffness parameter k_0 (c) for the law 7. The left $y-axis$ shows the error bar of the standard deviation (σ), while the right $y-axis$ the percentage variation of mean distribution (μ). Dotted line represents the mean reference value among all five mean va$Error\ \sigma$lues evaluated for each Device.

the device number and the parameter number, respectively. Dimensions of n, hence, the size of each component of the vector α, depends on the considered constitutive law. Moreover, apex $j = [1, 2, \ldots, 9]$ represents the different constitutive laws of the investigated numerical models.

For instance, an explicit representation of vector α, according to the symbology adopted for each parameter's law and introduced in Table 4, assumes the following form:

$$\alpha = \left(\begin{bmatrix} C^{(1)}_{dev.1} \\ C^{(1)}_{dev.2} \\ C^{(1)}_{dev.3} \\ C^{(1)}_{dev.4} \\ C^{(1)}_{dev.5} \end{bmatrix} \begin{bmatrix} C^{(2)}_{dev.1} & \alpha^{(2)}_{dev.1} \\ C^{(2)}_{dev.2} & \alpha^{(2)}_{dev.2} \\ C^{(2)}_{dev.3} & \alpha^{(2)}_{dev.3} \\ C^{(2)}_{dev.4} & \alpha^{(2)}_{dev.4} \\ C^{(2)}_{dev.5} & \alpha^{(2)}_{dev.5} \end{bmatrix} \cdots \begin{bmatrix} C^{(9)}_{dev.1} & \alpha^{(9)}_{dev.1} & \beta^{(9)}_{dev.1} \\ C^{(9)}_{dev.2} & \alpha^{(9)}_{dev.2} & \beta^{(9)}_{dev.2} \\ C^{(9)}_{dev.3} & \alpha^{(9)}_{dev.3} & \beta^{(9)}_{dev.3} \\ C^{(9)}_{dev.4} & \alpha^{(9)}_{dev.4} & \beta^{(9)}_{dev.4} \\ C^{(9)}_{dev.5} & \alpha^{(9)}_{dev.5} & \beta^{(9)}_{dev.5} \end{bmatrix} \right) \tag{20}$$

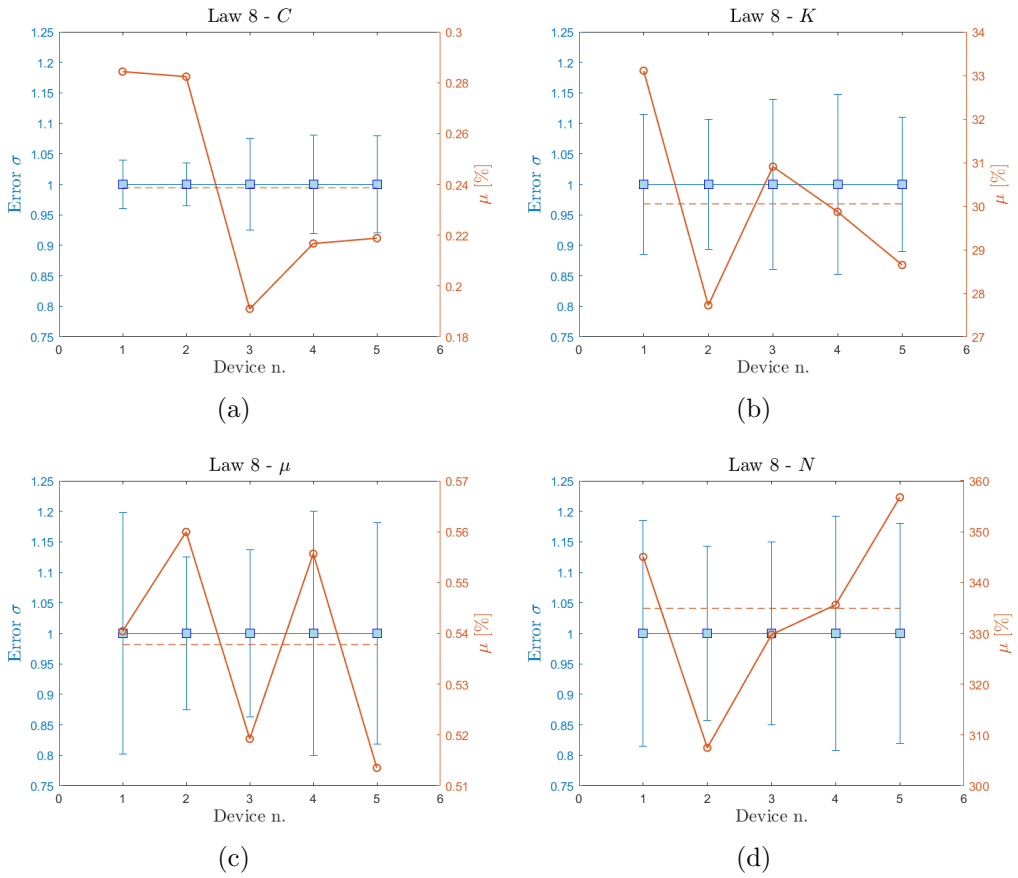

Figure 12: Normalized standard deviation and mean distribution of the identified damping C (a), stiffness parameter k_0 (b), friction coefficient μ and normal contact force N for the law 8. The left $y-axis$ shows the error bar of the standard deviation (σ),while the right $y-axis$ the percentage variation of mean distribution (μ). Dotted line represents the mean reference value among all five mean values evaluated for each Device.

At first, percentage variations of each parameter, with respect to a reference value, are evaluated for each considered law. For example, the percentage variation, $\Delta_1^{(j)}$, of the parameter $n = 1$ of the generic constitutive law j will be written as following:

$$\Delta_1^{(j)} = max(abs(\{\Delta_{11}^{(j)}, \Delta_{21}^{(j)}, \dots, \Delta_{m1}^{(j)}\})) \tag{21}$$

$$\textbf{where} \quad \Delta_{m1} = \frac{\alpha_{m1} - \alpha_{\mu 1}}{\alpha_{\mu 1}}. \tag{22}$$

For clarity purposes, the maximum percentage variation, Δ, evaluated for each device, is expressed for the parameter $n = 1$ as reported in Eq.21. The generic percentage variation, $\Delta_{m1}^{(j)}$, is a measure of the dispersion of the parameter α of a specific device m with respect to a reference value expressed by the mean, $\alpha_{\mu 1}$, of all α values evaluated for each device. Though each device exhibits similar properties, the authors focused on investigating the variability of a specific parameter with respect to the average value evaluated among all the devices.

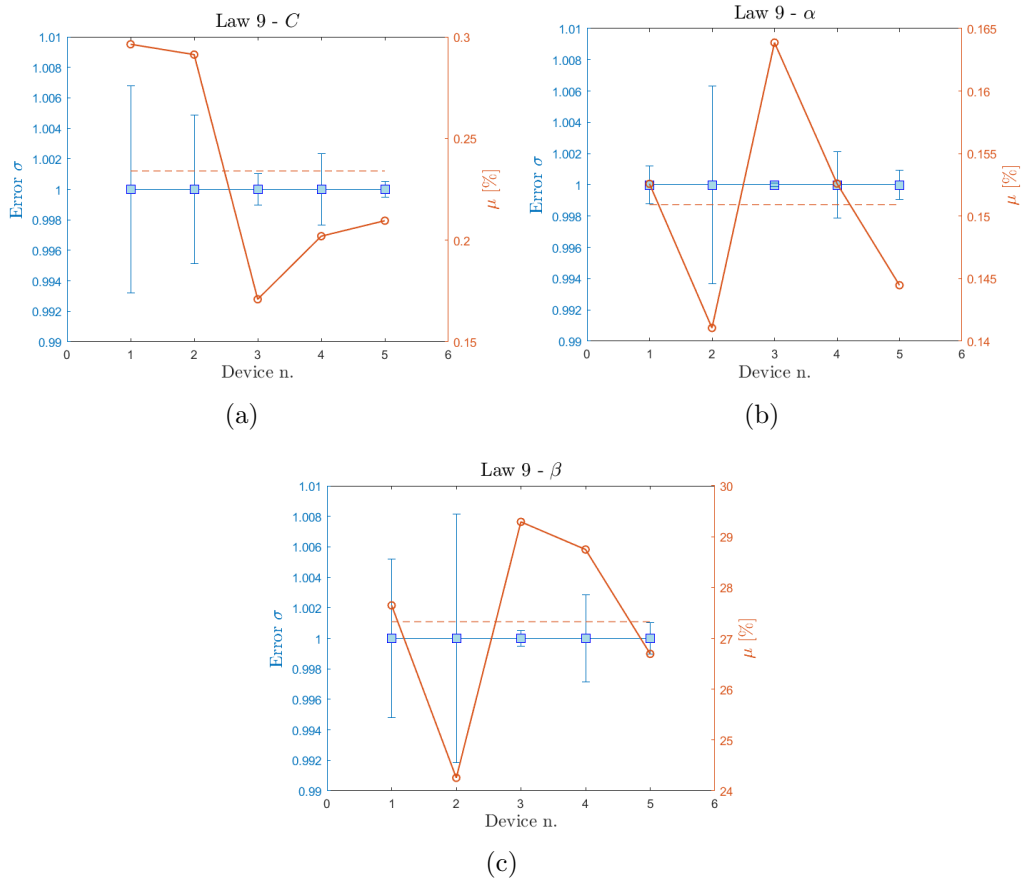

Figure 13: Normalized standard deviation and mean distribution of the identified damping C (a), exponent parameter α (b) and β (c) for the law 9. The left $y-axis$ shows the error bar of the standard deviation (σ), while the right $y-axis$ the percentage variation of mean distribution (μ). Dotted line represents the mean reference value among all five mean values evaluated for each Device.

In this way, a measure of the accuracy provided by that parameter in a specific law can be detected. This procedure is applied for each parameter of each investigated constitutive law. In this way, for the generic law j, the value β_j can be evaluated as:

$$\beta_j = \frac{\sum \Delta_n^{(j)}}{n_n}. \tag{23}$$

The no-dimensional value β can be assumed as a robustness index corresponding to the generic law j. This value is obtained, for each law, by summing all the percentage variations of the n parameter which govern that specific constitutive law.

With the aim to summarize general outcomes in a single plot where a measure of accuracy and robustness of each law is given, Fig.14 depicts the OF parameter, evaluated as the mean of all twenty optimization runs and among all devices, and index β on the Y and X-axis, respectively. Increasing the accuracy of a model (lower values of OF), a decrease in the

overall robustness (high values of β) is observed. Due to the opposite trend of these indices, a Pareto Front plot is developed and the best performer among all investigated models is identified.

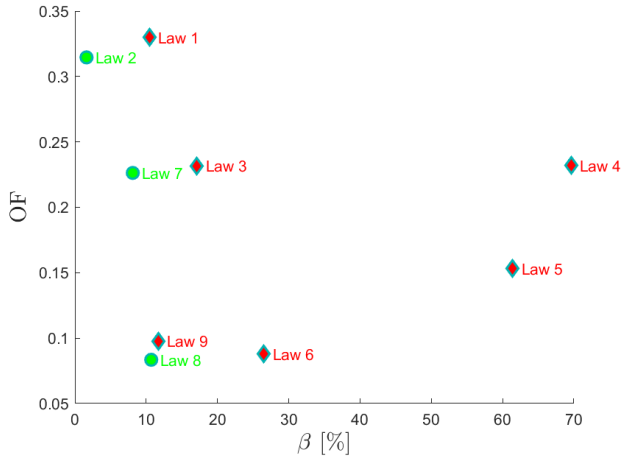

Figure 14: Accuracy (OF) vs robustness (β) Pareto front. The best constitutive laws as a good compromise between accuracy and robustness are marked in green while the dominated solutions are reported in red. The trend realized by connecting the green points represents the Pareto front of the non-dominated solutions.

In the scatter representation, data are clustered into two groups by using green and red colours. Green points represent the good compromise between accuracy and robustness features, while red points are the dominated-solution of the optimization problem. In other words, by selecting one of the red marked points, it is always possible to identify whatever solutions, among the green ones, which can be preferred in terms of accuracy or robustness (or both). Therefore, those models corresponding to green points lie in a Pareto Front, and all performers, identified by the couple $[\beta, OF]$, which belong the right side can be considered dominated solutions of the optimization problem.

For instance, Law#2 represents the best performer in terms of dispersion, hence, it represents the best model in which identified parameters contribute to obtaining the lowest value of β among the investigated models. On the contrary, due to the algebraic nature of Law#2, it is not the most effective with respect to the capability of reproducing the real behaviour of experimental outputs. Indeed, solutions, such as Law#7 or Law#8, can be preferred for the lower OF.

An interesting consideration can be pointed out by comparing the gain and loss in terms of OF and β from Law#2 to Law#8. Focusing on Fig.14, it is quite evident that the loss in terms of parameters variability is negligible if compared with the gain in terms of OF

of Law#8. This is evident in the comparison between experimental and numerical cycles depicted in Fig.s3-(i),(l) and Fig.s3-(o),(p).

8. Conclusions and future developments

In the present paper, an identification procedure for the evaluation of the optimal parameters of nine different FVD numerical models has been implemented. The procedure has been performed via metaheuristic technique and Genetic Algorithm suitably modified and adapted to the final scope. Data derived from an experimental campaign has been adopted and five FVD devices, with the same characteristics, have been tested in dynamic conditions. An identification scheme has been developed to compare the experimental and analytical values of the forces experienced by the device series under investigation. A comparison of the optimal numerical hysteresis cycles against the laboratory outcomes, for each adopted law, has been shown. Moreover, a statistic analysis has been conducted and trends and patterns have been highlighted. Generally, results shown how differential laws better fit with experimental curves. Specifically, Law#8 and Law#9 exhibited a high level of accuracy with a moderate dispersion among identified parameters. Finally, the Pareto front representation has been adopted aiming to identify the set of best performers both in terms of laws' accuracy and robustness.

Law#2 has been identified as that one with the highest robustness with a significant loss in terms of accuracy. However, differential models as Law#7 and, especially, Law#8, can be considered the most promising models for their low OF values even though a minimal loss in terms of overall dispersion has been assessed.

Extending the experimental campaign could be useful to consolidate the obtained results. However, it would involve obvious implementation difficulties. Therefore, future development of this study will involve the procedure generalization to a higher number of devices by numerical simulation, introducing parameters' variability (e.g., fluid characteristics, tolerances in the mechanical components). This virtual test campaign, supported by a limited number of real tests, would also allow the study of multiple loading patterns to analyze the effectiveness of the identified models under different operating conditions.

Acknowledgments

The research leading to these results has received funding from the European Research Council under the Grant agreement ID: 101007595 of the project ADDOPTML, MSCA RISE 2020 Marie Skodowska Curie Research and Innovation Staff Exchange (RISE). SISMALAB in Crispiano TA is gratefully acknowledged for providing the test data.

References

[1] M. Martinez-Paneda, A. Elghazouli, An integrated damping system for tall buildings, Structural Design of Tall and Special Buildings 29 (7), cited By 5 (2020). doi:10.1002/tal.1724.

[2] T. Roy, V. Matsagar, Effectiveness of passive response control devices in buildings under earthquake and wind during design life, Structure and Infrastructure Engineering 15 (2) (2019) 252–268, cited By 24. doi:10.1080/15732479.2018.1547768.

[3] J. Zhu, W. Zhang, K. Zheng, H. Li, Seismic design of a long-span cable-stayed bridge with fluid viscous dampers, Practice Periodical on Structural Design and Construction 21 (1), cited By 35 (2016). doi:10.1061/(ASCE)SC.1943-5576.0000262.

[4] P. Azarsa, M. Hosseini, S. Ahmadi, N. Rao, Enhanced seismic resistance of steel buildings using viscous fluid dampers, International Journal of Civil Engineering and Technology 7 (6) (2016) 90–105, cited By 7.

[5] Z.-Q. Jiang, Y.-T. Kang, X.-C. Liu, K.-K. Cheng, X. Chen, Experimental study of an earthquake-resilient prefabricated opening-web steel channel beam-to-column joint with flange cover plates, Engineering Structures 221, cited By 4 (2020). doi:10.1016/j.engstruct.2020.111054.

[6] L. Kibriya, C. Málaga-Chuquitaype, M. Kashani, N. Alexander, Nonlinear dynamics of self-centring rocking steel frames using finite element models, Soil Dynamics and Earthquake Engineering 115 (2018) 826–837, cited By 22. doi:10.1016/j.soildyn.2018.09.036.

[7] M. Rahman, S. Chang, D. Kim, Multiple wall dampers for multi-mode vibration control of building structures under earthquake excitation, Structural Engineering and Mechanics 63 (4) (2017) 537–549, cited By 4. doi:10.12989/sem.2017.63.4.537.

[8] B. Silwal, R. Michael, O. Ozbulut, A superelastic viscous damper for enhanced seismic performance of steel moment frames, Engineering Structures 105 (2015) 152–164, cited By 71. doi:10.1016/j.engstruct.2015.10.005.

[9] E. Booth, Dealing with earthquakes: the practice of seismic engineering 'as if people mattered', Bulletin of Earthquake Engineering 16 (4) (2018) 1661–1724, cited By 12. doi:10.1007/s10518-017-0302-8.

[10] G. Del Gobbo, A. Blakeborough, M. Williams, Improving total-building seismic performance using linear fluid viscous dampers, Bulletin of Earthquake Engineering 16 (9) (2018) 4249–4272, cited By 23. doi:10.1007/s10518-018-0338-4.

[11] W.-H. Lin, A. Chopra, Earthquake response of elastic sdf systems with non-linear fluid viscous dampers, Earthquake Engineering and Structural Dynamics 31 (9) (2002) 1623–1642, cited By 182. doi:10.1002/eqe.179.

[12] F. Malik, C. Kolay, Optimal parameters for tall buildings with a single viscously damped outrigger considering earthquake and wind loads, Structural Design of Tall and Special BuildingsCited By 0 (2023). doi:10.1002/tal.2003.

[13] Y. Nakamura, R. Matsumura, Cross-story installation of viscous dampers in timber frame houses for earthquake damage reduction, Frontiers in Built Environment 8, cited By 0 (2022). doi:10.3389/fbuil.2022.1037832.

[14] R. Flores-Mendoza, A. Pozos-Estrada, R. Gómez, Comparative study of the damage cost of reinforced concrete buildings with and without nonlinear viscous dampers subjected to seismic loading, Frontiers in Built Environment 8, cited By 0 (2022). doi:10.3389/fbuil.2022.953193.

[15] C. Su, J. Xian, Topology optimization of non-linear viscous dampers for energy-dissipating structures subjected to non-stationary random seismic excitation, Struc-

tural and Multidisciplinary Optimization 65 (7), cited By 2 (2022). doi:10.1007/s00158-022-03281-2.

[16] M. Martinez-Paneda, A. Elghazouli, Optimal application of fluid viscous dampers in tall buildings incorporating integrated damping systems, Structural Design of Tall and Special Buildings 30 (17), cited By 0 (2021). doi:10.1002/tal.1892.

[17] Y. Ikeda, M. Yamamoto, T. Furuhashi, H. Kurino, Recent research and development of structural control in japan, Japan Architectural Review 2 (3) (2019) 219–225. doi:10.1002/2475-8876.12081.

[18] M. Willford, A. Whittaker, R. Klemencic, A. Wood, C. on Tall Buildings, U. Habitat, Recommendations for Seismic Design of High-Rise Buildings: A Consensus Document - CTBUH Seismic Working Group, Council on Tall Buildings and Urban Habitat, 2008.

[19] M. Sharbatdar, S. H. Vaez, G. G. Amiri, H. Naderpour, Seismic response of base-isolated structures with lrb and fps under near fault ground motions, Procedia Engineering 14 (2011) 3245–3251, the Proceedings of the Twelfth East Asia-Pacific Conference on Structural Engineering and Construction. doi:https://doi.org/10.1016/j.proeng.2011.07.410.

[20] D. De Domenico, G. Ricciardi, Earthquake protection of structures with nonlinear viscous dampers optimized through an energy-based stochastic approach, Engineering Structures 179 (2019) 523–539. doi:https://doi.org/10.1016/j.engstruct.2018.09.076.

[21] M. Ismail, J. Rodellar, G. Carusone, M. Domaneschi, L. Martinelli, Characterization, modeling and assessment of roll-n-cage isolator using the cable-stayed bridge benchmark, Acta Mechanica 224 (3) (2013) 525–547. doi:10.1007/s00707-012-0771-4.

[22] G. De Mari, M. Domaneschi, M. Ismail, L. Martinelli, J. Rodellar, Reduced-order coupled bidirectional modeling of the roll-n-cage isolator with application to the updated bridge benchmark, Acta Mechanica 226 (10) (2015) 3533–3553. doi:10.1007/s00707-015-1394-3.

[23] D. Hahm, S.-Y. Ok, W. Park, H.-M. Koh, K.-S. Park, Cost-effectiveness evaluation of an mr damper system based on a life-cycle cost concept, KSCE Journal of Civil Engineering 17 (1) (2013) 145–154, cited By 10. doi:10.1007/s12205-013-1244-6.

[24] Y. Liu, K. Wang, O. Mercan, H. Chen, P. Tan, Experimental and numerical studies on the optimal design of tuned mass dampers for vibration control of high-rise structures, Engineering Structures 211, cited By 21 (2020). doi:10.1016/j.engstruct.2020.110486.

[25] M. Hochrainer, F. Ziegler, Control of tall building vibrations by sealed tuned liquid column dampers, Structural Control and Health Monitoring 13 (6) (2006) 980–1002, cited By 77. doi:10.1002/stc.90.

[26] T. Soong, B. Spencer Jr., Supplemental energy dissipation: State-of-the-art and state-of-the-practice, Engineering Structures 24 (3) (2002) 243–259, cited By 937. doi:10.1016/S0141-0296(01)00092-X.

[27] M. Domaneschi, Feasible control solutions of the asce benchmark cable-stayed bridge, Structural Control and Health Monitoring 17 (6) (2010) 675–693, cited By 43. doi:10.1002/stc.346.

[28] M. Domaneschi, Simulation of controlled hysteresis by the semi-active bouc-wen model, Computers and Structures 106-107 (2012) 245–257, cited By 43. doi:10.1016/j.compstruc.2012.05.008.

[29] S. Moradpour, M. Dehestani, Optimal ddbd procedure for designing steel structures with nonlinear fluid viscous dampers, Structures 22 (2019) 154–174, cited By 31. doi:10.1016/j.istruc.2019.08.005.

[30] H. Lak, S. Zahrai, Self-heating of viscous dampers under short- amp; long-duration loads: Experimental observations and numerical simulations, Structures 48 (2023) 275–287, cited By 0. doi:10.1016/j.istruc.2022.12.079.

[31] M. Domaneschi, L. Martinelli, E. Po, Control of wind buffeting vibrations in a suspen-

sion bridge by tmd: Hybridization and robustness issues, Computers and Structures 155 (2015) 3–17, cited By 55. doi:10.1016/j.compstruc.2015.02.031.

[32] F. Perotti, M. Domaneschi, S. De Grandis, The numerical computation of seismic fragility of base-isolated nuclear power plants buildings, Nuclear Engineering and Design 262 (2013) 189–200, cited By 85. doi:10.1016/j.nucengdes.2013.04.029.

[33] R. Greco, J. Avakian, G. Marano, A comparative study on parameter identification of fluid viscous dampers with different models, Archive of Applied Mechanics 84 (8) (2014) 1117–1134, cited By 14. doi:10.1007/s00419-014-0869-3.

[34] R. Greco, G. Marano, Identification of parameters of maxwell and kelvin-voigt generalized models for fluid viscous dampers, JVC/Journal of Vibration and Control 21 (2) (2015) 260–274, cited By 44. doi:10.1177/1077546313487937.

[35] B. Chalarca, A. Filiatrault, D. Perrone, Parametric study and prediction models of the seismic response of single-degree-of-freedom structural systems equipped with maxwell material fluid viscous dampers, Structures 43 (2022) 388–406, cited By 2. doi:10.1016/j.istruc.2022.06.051.

[36] N. Pollini, O. Lavan, O. Amir, Minimum-cost optimization of nonlinear fluid viscous dampers and their supporting members for seismic retrofitting, Earthquake Engineering and Structural Dynamics 46 (12) (2017) 1941–1961, cited By 59. doi:10.1002/eqe.2888.

[37] O. Vasile, M. Bugaru, A new modeling approach for viscous dampers using an extended kelvin–voigt rheological model based on the identification of the constitutive law's parameters, Computation 11 (1), cited By 0 (2023). doi:10.3390/computation11010003.

[38] M. D. I. E. D. TRASPORTI, Aggiornamento delle norme tecniche per le costruzioni (in italian), Gazzetta Ufficiale Serie Generale della Repubblica Italiana (42) (2018).

[39] M. Ismail, F. Ikhouane, J. Rodellar, The hysteresis bouc-wen model, a survey, Archives of Computational Methods in Engineering 16 (2) (2009) 161–188, cited By 557. doi:10.1007/s11831-009-9031-8.

[40] S. Park, M. Lackner, P. Pourazarm, A. Rodríguez Tsouroukdissian, J. Cross-Whiter, An investigation on the impacts of passive and semiactive structural control on a fixed bottom and a floating offshore wind turbine, Wind Energy 22 (11) (2019) 1451–1471, cited By 26. doi:10.1002/we.2381.

[41] R. Jiménez, L. Álvarez Icaza, Lugre friction model for a magnetorheological damper, Structural Control and Health Monitoring 12 (1) (2005) 91–116, cited By 107. doi:10.1002/stc.58.

[42] F. Yang, R. Sedaghati, E. Esmailzadeh, Development of lugre friction model for large-scale magnetoĝ€ "rheological fluid dampers, Journal of Intelligent Material Systems and Structures 20 (8) (2009) 923–937, cited By 18. doi:10.1177/1045389X08099660.

[43] L.-Y. Lu, G.-L. Lin, C.-H. Lin, A unified analysis model for energy dissipation devices used in seismic structures, Computer-Aided Civil and Infrastructure Engineering 24 (1) (2009) 41–61, cited By 18. doi:10.1111/j.1467-8667.2008.00567.x.

[44] A. Ghaemmaghami, O.-S. Kwon, Nonlinear modeling of mdof structures equipped with viscoelastic dampers with strain, temperature and frequency-dependent properties, Engineering Structures 168 (2018) 903–914, cited By 21. doi:10.1016/j.engstruct.2018.04.037.

[45] M. Banazadeh, A. Ghanbari, R. Ghanbari, Seismic performance assessment of steel moment-resisting frames equipped with linear and nonlinear fluid viscous dampers with the same damping ratio, Journal of Constructional Steel Research 136 (2017) 215–228, cited By 21. doi:10.1016/j.jcsr.2017.05.022.

[46] Z. Lu, Z. Wang, Y. Zhou, X. Lu, Nonlinear dissipative devices in structural vibration control: A review, Journal of Sound and Vibration 423 (2018) 18–49, cited By 186. doi:10.1016/j.jsv.2018.02.052.

[47] G. Terenzi, Dynamics of sdof systems with nonlinear viscous damping, Journal of Engineering Mechanics 125 (8) (1999) 956–963, cited By 91. doi:10.1061/(ASCE)0733-9399(1999)125:8(956).

[48] S. Erlicher, N. Point, Thermodynamic admissibility of bouc-wen type hysteresis models, Comptes Rendus - Mecanique 332 (1) (2004) 51–57, cited By 62. doi:10.1016/j.crme.2003.10.009.

[49] M. Ismail, F. Ikhouane, J. Rodellar, The hysteresis bouc-wen model, a survey, Archives of Computational Methods in Engineering 16 (2) (2009) 161–188, cited By 557. doi:10.1007/s11831-009-9031-8.

[50] C. de Wit, P. Lischinsky, K. Åström, H. Olsson, A new model for control of systems with friction, IEEE Transactions on Automatic Control 40 (3) (1995) 419–425, cited By 3019. doi:10.1109/9.376053.

[51] F. Casciati, M. Domaneschi, Semi-active electro-inductive devices: Characterization and modelling, JVC/Journal of Vibration and Control 13 (6) (2007) 815–838, cited By 35. doi:10.1177/1077546307077465.

[52] J. Holland, Genetic algorithms, Scientific American 267 (1) (1992) 66 – 72, cited by: 3165. doi:10.1038/scientificamerican0792-66.

Appendix A.

This section is devoted to the results derived by the optimization process. Mean (μ) and standard deviation (σ) for all design variables involved into the optimization process are calculated. Values of OF and identified value of parameters, for each law, are reported in table A.7 for completeness purposes.

Table A.7: Means (μ) and standard deviations (σ) of design variables and OFs

		Device 1		Device 2		Device 3		Device 4		Device 5	
		μ	σ	μ	σ	μ	σ	μ	σ	μ	σ
Law 1	**OF**	0.3074	$2.36\text{x}10^{-12}$	0.3057	$2.30\text{x}10^{-12}$	0.3463	$2.50\text{x}10^{-12}$	0.3450	$2.67\text{x}10^{-12}$	0.3454	$1.50\text{x}10^{-12}$
	C	0.7248	$1.47\text{x}10^{-09}$	0.6962	$1.07\text{x}10^{-09}$	0.5922	$4.01\text{x}10^{-09}$	0.6497	$1.84\text{x}10^{-09}$	0.6438	$3.26\text{x}10^{-09}$
Law 2	**OF**	0.2925	$3.46\text{x}10^{-04}$	0.2928	$2.19\text{x}10^{-04}$	0.3279	$3.85\text{x}10^{-04}$	0.3295	$3.04\text{x}10^{-04}$	0.3303	$8.19\text{x}10^{-04}$
	C	1.9944	0.0476	1.9657	0.0378	1.9946	0.0052	1.9715	0.0434	1.9698	0.0128
	α	0.8343	$4.10\text{x}10^{-03}$	0.8282	$3.30\text{x}10^{-03}$	0.7981	$4.33\text{x}10^{-04}$	0.8174	$3.70\text{x}10^{-03}$	0.8135	$1.10\text{x}10^{-03}$
Law 3	**OF**	0.2205	$5.09\text{x}10^{-05}$	0.2173	$1.95\text{x}10^{-05}$	0.2484	$1.08\text{x}10^{-05}$	0.2379	$1.03\text{x}10^{-05}$	0.2348	$3.37\text{x}10^{-05}$
	C	1.8913	$6.36\text{x}10^{-02}$	1.1743	$1.22\text{x}10^{-02}$	1.9405	$3.26\text{x}10^{-02}$	1.9548	$1.37\text{x}10^{-02}$	1.7877	0.12
	α	0.8337	$5.40\text{x}10^{-03}$	0.9047	$1.70\text{x}10^{-03}$	0.7969	$2.70\text{x}10^{-03}$	0.8084	$1.10\text{x}10^{-03}$	0.8221	$1.09\text{x}10^{-02}$
	K_1	2.1694	$9.80\text{x}10^{-03}$	2.1865	$3.80\text{x}10^{-03}$	2.2908	$3.60\text{x}10^{-02}$	2.5945	$3.90\text{x}10^{-03}$	2.5687	$3.15\text{x}10^{-02}$
Law 4	**OF**	0.2204	$1.91\text{x}10^{-04}$	0.2173	$6.11\text{x}10^{-05}$	0.2486	$1.47\text{x}10^{-04}$	0.2380	$9.99\text{x}10^{-05}$	0.2348	$6.24\text{x}10^{-05}$
	C	1.8315	$8.73\text{x}10^{-02}$	1.1827	$3.15\text{x}10^{-02}$	1.9414	$3.17\text{x}10^{-02}$	1.8873	$6.38\text{x}10^{-02}$	1.8029	$7.75\text{x}10^{-02}$
	α	0.8391	$4.10\text{x}10^{-03}$	0.9036	$3.30\text{x}10^{-03}$	0.7969	$4.33\text{x}10^{-04}$	0.8145	$3.70\text{x}10^{-03}$	0.8206	$1.10\text{x}10^{-03}$
	K_1	2.1910	$3.05\text{x}10^{-02}$	2.1904	$6.30\text{x}10^{-03}$	2.2975	$1.52\text{x}10^{-02}$	2.5978	$9.80\text{x}10^{-03}$	2.5611	$1.50\text{x}10^{-02}$
	K_2	0.0037	$11.0\text{x}10^{-04}$	0.0003	$2.90\text{x}10^{-04}$	0.0008	$4.47\text{x}10^{-04}$	0.0006	$4.28\text{x}10^{-04}$	0.0002	$1.37\text{x}10^{-04}$

		Device 1		Device 2		Device 3		Device 4		Device 5	
		μ	σ	μ	σ	μ	σ	μ	σ	μ	σ
	OF	0.1443	$1.02\text{x}10^{-04}$	0.1447	$7.03\text{x}10^{-05}$	0.1631	$3.13\text{x}10^{-05}$	0.1540	$2.67\text{x}10^{-05}$	0.1599	$3.29\text{x}10^{-04}$
	C	0.7295	0.0120	0.7538	0.0149	1.5499	0.0439	0.9060	0.0140	1.0592	0.0125
Law 5	α	0.9961	0.0027	0.9840	0.0032	0.8364	0.0047	0.9408	0.0025	0.9135	0.0021
	K	$1.51\text{x}10^{-06}$	$4.64\text{x}10^{-07}$	$3.07\text{x}10^{-06}$	$0.11\text{x}10^{-07}$	$2.11\text{x}10^{-06}$	$4.14\text{x}10^{-07}$	$9.70\text{x}10^{-06}$	$0.22\text{x}10^{-07}$	$0.20\text{x}10^{-06}$	$0.03\text{x}10^{-07}$
	β	4.9415	0.0727	4.7419	0.0813	4.8263	0.0557	4.4542	0.0655	4.3398	0.1647
	OF	0.0872	$1.14\text{x}10^{-04}$	0.0776	$2.05\text{x}10^{-05}$	0.0971	$7.22\text{x}10^{-05}$	0.0902	$5.85\text{x}10^{-05}$	0.0880	$1.65\text{x}10^{-04}$
	C	0.2999	$3.05\text{x}10^{-04}$	0.2941	$7.51\text{x}10^{-04}$	0.2057	$8.23\text{x}10^{-04}$	0.2295	$3.86\text{x}10^{-04}$	0.2275	$14.0\text{x}10^{-04}$
Law 6	K	30.0	0.0081	30.0	0.0042	30.0	0.0027	30.0	0.0058	30.0	0.0072
	α	$83.9\text{x}10^{-04}$	0.0305	$43.6\text{x}10^{-04}$	0.0063	$4.22\text{x}10^{-04}$	0.0152	$2.35\text{x}10^{-04}$	0.0098	$3.83\text{x}10^{-04}$	0.0150
	β	0.0842	$53.7\text{x}10^{-04}$	0.0881	$1.27\text{x}10^{-04}$	0.0911	$1.36\text{x}10^{-04}$	0.0843	$1.02\text{x}10^{-04}$	0.0845	$3.04\text{x}10^{-04}$
	OF	0.2336	$7.5\text{x}10^{-03}$	0.2419	$7.7\text{x}10^{-03}$	0.2188	$5.8\text{x}10^{-03}$	0.2179	$6.8\text{x}10^{-03}$	0.2192	$7.6\text{x}10^{-03}$
	C	6.0935	1.9256	6.2724	2.2382	5.3142	1.6503	5.9110	1.9019	6.3351	2.0116
Law 7	α	0.1569	0.0556	0.1507	0.0554	0.1486	0.0431	0.1513	0.0558	0.1391	0.0486
	K	115.67	18.726	118.15	15.562	102.65	16.546	107.81	17.240	105.76	19.306
	β	0.3466	0.0531	0.3278	0.0466	0.3080	0.0548	0.3171	0.0552	0.3196	0.0604

		Device 1		Device 2		Device 3		Device 4		Device 5	
		μ	σ	μ	σ	μ	σ	μ	σ	μ	σ
	OF	0.0902	$6.2\text{x}10^{-03}$	0.0779	$6.0\text{x}10^{-03}$	0.0875	$7.5\text{x}10^{-03}$	0.0814	$7.7\text{x}10^{-03}$	0.0802	$4.8\text{x}10^{-03}$
	C	0.2844	0.0114	0.2824	0.0099	0.1910	0.0144	0.2167	0.0175	0.2188	0.0175
Law 8	K	33.108	3.7877	27.724	2.9511	30.907	4.3087	29.569	4.3901	28.649	3.1568
	μ	0.5404	0.1069	0.5599	0.0703	0.5193	0.0710	0.5557	0.1116	0.5135	0.0934
	N	345.05	63.713	307.48	43.920	329.76	49.245	335.62	64.503	356.76	64.199
	OF	0.0934	$5.43\text{x}10^{-05}$	0.0896	$2.07\text{x}10^{-05}$	0.1047	$2.25\text{x}10^{-07}$	0.1006	$1.42\text{x}10^{-06}$	0.1002	$7.31\text{x}10^{-07}$
	C	0.2964	$20.0\text{x}10^{-04}$	0.2913	$14.0\text{x}10^{-04}$	0.1710	$1.78\text{x}10^{-04}$	0.2020	$4.75\text{x}10^{-04}$	0.2096	$1.12\text{x}10^{-04}$
Law 9	α	0.1526	$1.83\text{x}10^{-04}$	0.1411	$8.93\text{x}10^{-04}$	0.1639	$0.19\text{x}10^{-04}$	0.1526	$3.23\text{x}10^{-04}$	0.1445	$1.33\text{x}10^{-04}$
	β	27.649	0.1439	24.256	0.1972	29.292	0.0150	28.748	0.0821	26.695	0.0276

Appendix B.

In this section, numerical and experimental Time-history curves are reported for comparison purposes. All plots are referred to device 2 which exhibits the best results in terms of accuracy (OF). In Fig.s 3 (a)-(i), experimental ($F_{experimental}$ vs t_{vec}) and numerical curves ($F_{numerical}$ vs t_{vec}) are depicted for each law, rispectively. Generally, as recognized for

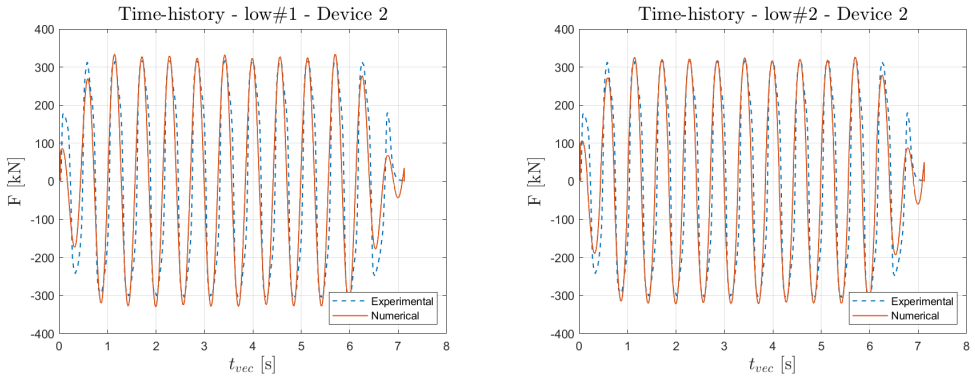

(a)

(b)

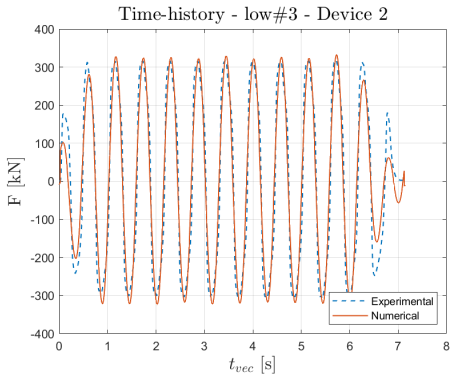

(c)

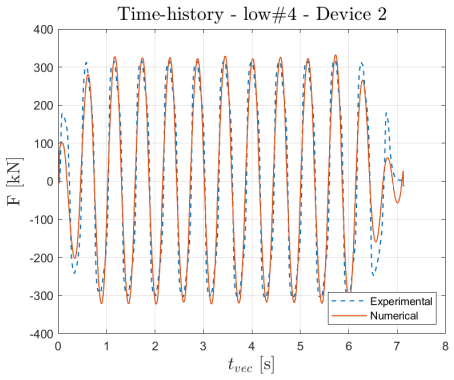

(d)

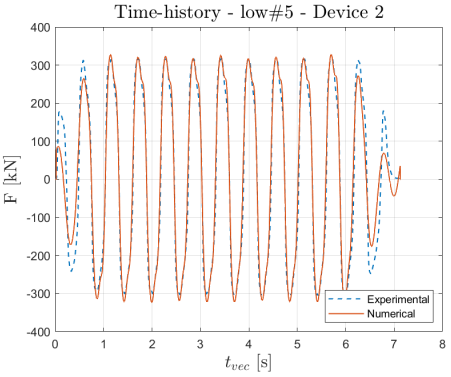

(e)

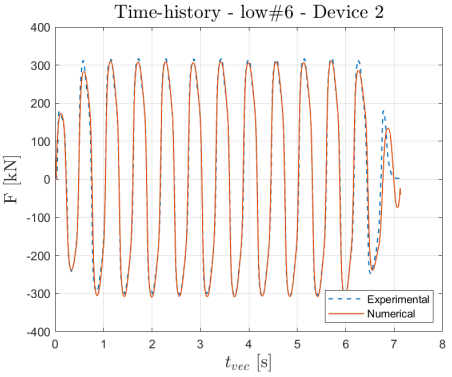

(f)

the optimal hysteresis cycles discussed in section 5, best matches between experimental and numerical curves are observed by differential law (from law#6 up to law#9). Despite to the first five models, differential models fit better specifically at the peaks of each cycle. In

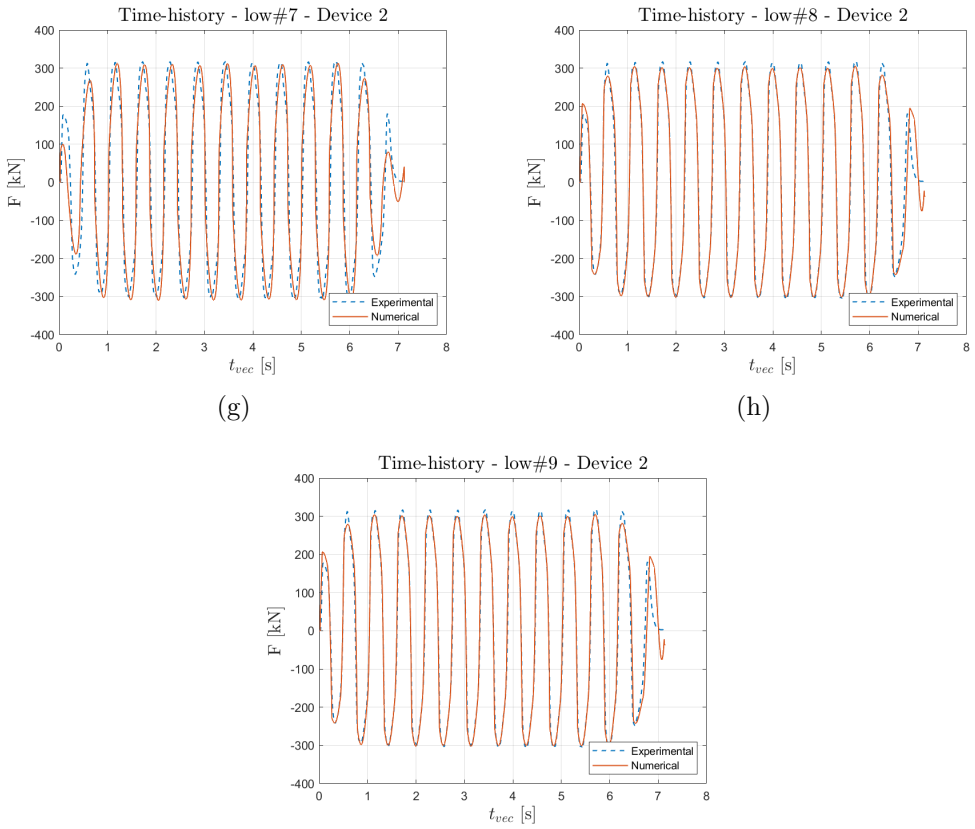

Figure B.15: Comparison between experimental (dotted blu line) and numerical (solid red line) time-history is depicted for each investigated law. Recorded experimental load, $F_{experimental}$, and numerical load, $F_{numerical}$, are reported along $Y - axis$ while t_{vec}, along $X - axis$, is representative of both time-step acquisition and numerical integration.

particular, law#8 and law#9 show a good grade of match not only at the stage of maximum load but during the transient phase too.

On the other hand, though numerical curves derived by no differential model (from law#1 up to law#5) show a generic good grade of match with experimental curve, numerical noises are recognized at the peak value of each cycle. By observing the plot related to law#5, this phenomenon becomes more evident. Moreover, all these models are not capable of taking the initial and final transient phases.